Eur. Phys. J. A **21**, 37–55 (2004)
DOI 10.1140/epja/i2003-10181-4

THE EUROPEAN PHYSICAL JOURNAL A

Investigations of the level scheme of ^{144}Gd and lifetimes in the quadrupole bands

R.M. Lieder[1,a], A.A. Pasternak[1,2], E.O. Podsvirova[1,2], A.D. Efimov[2], V.M. Mikhajlov[3], R. Wyss[4], Ts. Venkova[5], W. Gast[1], H.M. Jäger[1], L. Mihailescu[1], D. Bazzacco[6], S. Lunardi[6], R. Menegazzo[6], C. Rossi Alvarez[6], G. de Angelis[7], D.R. Napoli[7], T. Rząca-Urban[8], W. Urban[8], and A. Dewald[9]

[1] Institut für Kernphysik, Forschungszentrum Jülich, D-52425 Jülich, Germany
[2] A.F. Ioffe Physical Technical Institute RAS, RU-194021 St. Petersburg, Russia
[3] Physical Institute, St. Petersburg State University, RU-198904 St. Petersburg, Russia
[4] Royal Institute of Technology, Physics Department Frescati, S-10405 Stockholm, Sweden
[5] Institute of Nuclear Research and Nuclear Energy, Bulgarian Academy of Sciences, BG-1784 Sofia, Bulgaria
[6] Dipartimento di Fisica dell'Università and Istituto Nazionale di Fisica Nucleare, Sezione di Padova, I-35131 Padova, Italy
[7] Istituto Nazionale di Fisica Nucleare, Laboratori Nazionali di Legnaro, I-35020 Legnaro, Italy
[8] Institute of Experimental Physics, University of Warsaw, PL-00-681 Warszawa, Poland
[9] Institut für Kernphysik, Universität zu Köln, D-50937 Köln, Germany

Received: 5 June 2003 / Revised version: 10 December 2003 /
Published online: 23 July 2004 –
Communicated by D. Schwalm

Abstract. For a level scheme investigation of ^{144}Gd an experiment with the γ-spectrometer EUROBALL III has been carried out and lifetimes have been measured with the γ-spectrometer GASP using the Doppler-shift attenuation method. The high-spin states have been populated in these experiments by means of the ^{100}Mo(^{48}Ti,4n) reaction at 215 MeV and the ^{114}Cd(^{36}S,6n) reaction at $E = 182$ MeV, respectively. The known quadrupole band has been modified and a new one has been established. Reduced $E2$ transition probabilities $B(E2)$ were determined for seven members of these quadrupole bands. They show values between ≈ 60 and 130 W.u. and this considerable enhancement gives evidence for a significant nuclear deformation. A $(\pi h_{11/2})^2 \otimes (\nu h_{11/2})^{-2}$ configuration may be assigned to one of the quadrupole bands according to total Routhian surface calculations. The spin dependence of the $B(E2)$ values has been explained by IBM calculations involving high-spin quasiparticle excitations.

PACS. 21.10.Re Collective levels – 21.10.Tg Lifetimes – 21.60.Fw Models based on group theory – 27.60.+j
$90 \leq A \leq 149$

1 Introduction

High-spin rotational bands, built on states of large quadrupole deformation, have been extensively studied in the mass regions with $A \approx 130$ and $A \approx 150$. For the $A \approx 130$ region nuclear deformations of $\beta_2 \approx 0.35$–0.40 (highly deformed bands) and for the $A \approx 150$ region of $\beta_2 \approx 0.50$–0.60 (superdeformed bands) have been found [1]. One of the major open problems is to explore the transition between these two regions. Therefore, the band structures of the nuclei $^{142-144}$Gd situated in the transition region have been investigated. In ^{144}Gd five strongly populated superdeformed bands have been observed [2]. However, in ^{143}Gd only one weak superdeformed band has been established [3] indicating that the superdeformed bands move to higher excitation energies with decreasing neutron number, so that they are not populated anymore in the lighter Gd nuclei. The fact that highly deformed bands are absent in the heavier Gd isotopes whereas they exist in the light ones, is probably related to the development of triaxial shapes. In ^{142}Gd three low-lying quadrupole bands of positive parities have been found [4], the ground band and two bands based on 10^+ isomers of $\nu h_{11/2}^{-2}$ and $\pi h_{11/2}^2$ configurations [5], respectively. The latter one was observed up to $I = 34$ and shows two band crossings at $\hbar\omega \approx 0.38$ and 0.50 MeV caused by the $h_{9/2}$ and $i_{13/2}$ neutron orbitals, respectively, according to total Routhian surface (TRS) calculations [3]. Bands with similar features have been observed in ^{143,144}Gd. The alignment of the $i_{13/2}$ neutrons is predicted to drive the nuclear shape associated with the long stretched $E2$ cascades of $^{142-144}$Gd into a

[a] e-mail: r.lieder@fz-juelich.de

well-deformed, triaxial minimum ($\beta_2 = 0.25$, $\gamma = 26.5°$). For ^{139}Gd a highly deformed shape ($\beta_2 = 0.35$) already exists at low spins [6,7].

To understand the development of the shape of the Gd nuclei also the low-spin states have to be considered. For the low-spin states in the neutron-deficient Gd isotopes the deformation decreases with increasing neutron number and a spherical shell structure develops when the shell closure at $N = 82$ is approached. The shape transition is clearly visible when the level schemes of ^{142}Gd and ^{144}Gd are compared. In ^{142}Gd [4] a ground band is observed which has a structure resembling that of a vibrator or a rotor with a modest deformation. In contrast, ^{144}Gd [8] shows up to a spin $I \approx 18$, a structure which requires an explanation in terms of shell-model excitations. The transition from deformed to spherical-like structures appears to occur rather suddenly between $N = 78$ and 80. In order to investigate the development of the nuclear shape for the stretched $E2$ bands of $^{142-144}$Gd, lifetime measurements are required. In the present work lifetimes for ^{144}Gd have been determined. New structure information on the quadrupole bands in ^{144}Gd from an experiment with the γ-spectrometer EUROBALL III and lifetimes of several of their levels, obtained from a DSAM experiment at the γ-spectrometer GASP, are presented in sect. 3. For the interpretation of the results TRS calculations as well as calculations in the framework of a model employing collective quadrupole d-bosons of IBM and high-spin quasiparticle excitations have been performed as discussed in sect. 4.

2 Experimental methods

High-spin states in ^{144}Gd have been studied in the ^{100}Mo (^{48}Ti,4n) reaction at 215 MeV with EUROBALL III at the XTU tandem accelerator of the Laboratori Nazionali di Legnaro, Italy and as a result a number of irregular dipole as well as stretched quadrupole bands have been extended in comparison with previous investigations [8]. The EUROBALL III array was equipped with 14 CLUSTER detectors, 25 CLOVER detectors and 24 individual escape-suppressed Ge detectors (tapered detectors) [9]. The ^{100}Mo target consisted of two self-supporting metal foils with a total thickness of 1.05 mg/cm^2. Events were recorded when ≥ 6 unsuppressed Ge detectors fired in coincidence. Approximately $6.3 \cdot 10^9$ high-fold γ-events have been collected. The energy and efficiency calibrations of the EUROBALL III array have been carried out with ^{56}Co, ^{133}Ba and ^{152}Eu sources.

A γ-γ-γ cube has been sorted for the construction of the level scheme of ^{144}Gd. The presort of the data and the sorting into the cube have been carried out with the software package "Ana" [10]. In the presort the energy and time calibration has been carried out for all detectors used in the experiment. In the cube sort the composite detectors have been treated in the following way. Events from a CLUSTER detector were accepted i) when one Ge crystal fired, ii) when two neighbouring crystals fired or iii) when two neighbouring crystals and one non-neighbouring crystal fired. In cases ii) and iii) the energies of the neighbouring detectors were added up (addback mode). In case iii) the non-neighbouring detector was considered to have detected a second γ-ray from the target. Events from a CLOVER detector were accepted i) when one Ge crystal fired or ii) when two crystals fired in which case the energies were summed. For the Doppler-shift correction, carried out during the presort, the angles of the individual detectors with respect to the beam direction are used. From this it results that the correction for addback events is not exact since in case of a Compton-scattered γ-ray for both detectors involved in the event the angle of the detector in which the first hit occurs should be used. However, the error introduced in this way is ≤ 0.3 keV for 1 MeV γ-rays and hence about an order of magnitude smaller than the Doppler broadening.

For the interpretation of the complex band structure of the nucleus ^{144}Gd, which lies close to the semi doubly magic nucleus ^{146}Gd, the investigation of electromagnetic-transition probabilities is very important. In this work the results of a lifetime study using the Doppler-shift attenuation method (DSAM) for the 20^+ to 28^+ states of the quadrupole bands are presented. The ^{114}Cd(^{36}S,6n) reaction at $E = 182$ MeV has been used to populate the states of interest. The beam was provided by the XTU tandem accelerator of the Laboratori Nazionali di Legnaro, Italy. The target consisted of a 1.2 mg/cm^2 Cd foil (enrichment 99.19%) backed by a 1.2 mg/cm^2 Ta and a 55 mg/cm^2 Bi layer. The average velocity of the produced compound nuclei was $v/c = 2.5\%$. The γ-rays were detected using the GASP array which consists of 40 bismuth-germanate (BGO) suppressed Ge detectors and an 80-element BGO ball. Coincidence events were accepted when the number of responding Compton-suppressed Ge detectors was ≥ 2 and the BGO fold ≥ 8. A total of $1 \cdot 10^9$ γ-ray coincidence events have been collected. The Ge detectors of GASP are placed symmetrically with respect to the beam direction as follows: two each at 32° and 148°, four each at 36° and 144°, two each at 58° and 122°, four each at 60° and 120°, four each at 72° and 108°, and eight at 90°. The energy and efficiency calibrations of the GASP array have been carried out with ^{56}Co, ^{133}Ba and ^{152}Eu sources.

These data have been used for the lifetime analysis since under the experimental conditions the average angular momentum of the entry states of the 6n channel leading to ^{144}Gd is $\approx 35\hbar$ according to Monte Carlo simulation calculations and the calculated effective side-feeding times for high spins do not exceed ≈ 0.3 ps [11]. The data have been used before for a DSAM study of lifetimes in the superdeformed bands of ^{145}Gd populated in the 5n channel [12].

Several γ-γ matrices have been sorted for the lifetime analysis of transitions in ^{144}Gd. The presort of the data and the sorting into the matrices have been carried out with the software package "Ana" [10]. In the presort the energy and time calibration has been carried out for all detectors used in the experiment. The low-lying states in ^{145}Gd have lifetimes larger than a few ps and thus the

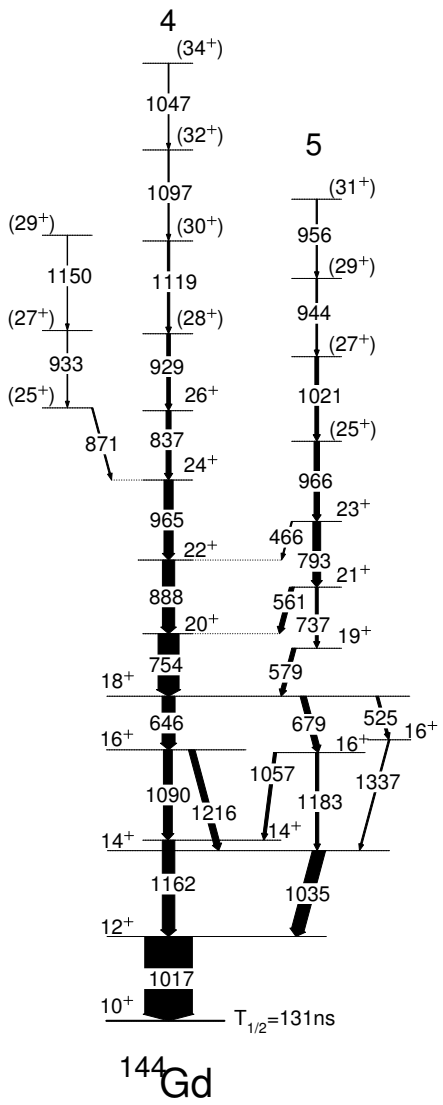

Fig. 1. Partial level scheme of ^{144}Gd based on the 10^+ isomer at 3434 keV. Uncertain spin-parity assignments are given in brackets. The widths of the arrows are proportional to the intensities of the transitions.

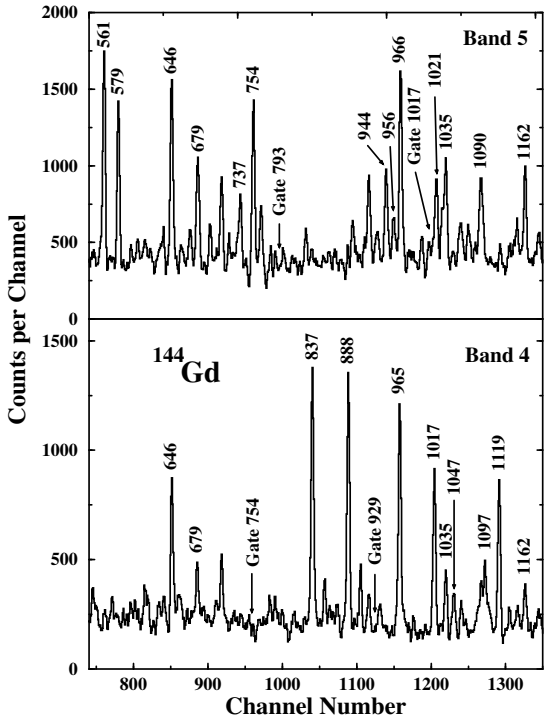

Fig. 2. Doubly gated concidence spectra for bands 4 and 5 in ^{144}Gd. The gates are indicated.

corresponding γ transitions showed no Doppler shift and were used for a reliable energy calibration. Seven matrices have been produced by sorting energies from any detector into one axis and the energies from detectors placed under a certain angle into the second axis of the respective matrix. Here, the detectors placed at angles differing by $\approx 2°$ (58°, 60° and 120°, 122°) or 4° (32°, 36° and 144°, 148°) have been sorted into one matrix each. Furthermore, one matrix has been produced where the energies from any detector have been sorted into both axes, to provide gated spectra of good statistics representing the sum over all angles. In order to enhance ^{144}Gd in the matrices, events with a fold $F = 8$–19 have been selected utilizing the γ-ray multiplicity information from the inner BGO ball.

3 Experimental results

3.1 Level scheme of ^{144}Gd

A partial level scheme above the 10^+ isomer at 3434 keV displaying the quadrupole bands in ^{144}Gd resulting from the analysis of the EUROBALL III data is shown in fig. 1. Spectra of the two quadrupole bands are shown in fig. 2. Table 1 contains spectroscopic information on the γ-ray transitions assigned to the quadrupole bands in ^{144}Gd.

A new band has been established, called band 5, which de-excites into the known quadrupole band 4 [8]. Some of the transitions in band 5 and those connecting it to band 4 have been previously observed but have been placed differently [8]. The order of the 579.0 and 737.0 keV transitions is based on intensity arguments. The transitions above the 23^+ level are ordered according to their intensities. The spin assignments are based on the previously measured DCO ratios [8] for the 561.3 keV ($R_{\rm DCO} = 0.70 \pm 0.14$) and 792.7 keV ($R_{\rm DCO} = 1.18 \pm 0.20$) transitions. In the experimental geometry, stretched quadrupole transitions have DCO ratios of 1 and stretched dipole transitions of 0.68. Therefore, the 561.3 keV γ-ray is considered as $\Delta I = 1$ transition and the band as stretched $E2$ cascade. A spin of 21 was proposed for the level de-excited by the 561.3 keV transition since no transition to the 18^+ level was observed which would be energetically favoured if the spin was 19. A positive parity was assigned to band 5 considering the measured lifetime of the $I = 23$ level (cf. table 2). Assuming $E1$ and $M1$ characters, respectively, for the 465.7 keV

Table 1. Energies, γ-ray intensities, DCO ratios and spin assignments of transitions in ^{144}Gd above the 10^+ isomer.

E_γ (keV)	Assignment	I_γ [a]	I_γ [b]	$R_{\rm DCO}$ [c]	Multipol.	Band
465.7 ± 0.3	$23^+ \rightarrow 22^+$	2.5 ± 0.4	2.2 ± 0.4			5
524.8 ± 0.3	$18^+ \rightarrow 16^+$	5.5 ± 1.0		1.25 ± 0.37	$E2$	
561.3 ± 0.2	$21^+ \rightarrow 20^+$	9.8 ± 1.1	9.7 ± 1.1	0.70 ± 0.14		5
579.0 ± 0.2	$19^+ \rightarrow 18^+$	8.8 ± 1.0	9.7 ± 1.1	1.05 ± 0.21	$E2$	5
646.1 ± 0.2	$18^+ \rightarrow 16^+$	27.2 ± 2.7		1.16 ± 0.18	$E2$	
679.3 ± 0.2	$18^+ \rightarrow 16^+$	12.6 ± 1.3		1.07 ± 0.19	$E2$	
737.0 ± 0.3	$21^+ \rightarrow 19^+$	6.1 ± 1.5	7.0 ± 1.7			5
754.3 ± 0.1	$20^+ \rightarrow 18^+$	44.0 ± 3.1	44.0 ± 3.1	1.07 ± 0.16	$E2$	4
792.7 ± 0.3	$23^+ \rightarrow 21^+$	16.4 ± 1.9	18.0 ± 2.1		$(E2)$	5
836.5 ± 0.3	$26^+ \rightarrow 24^+$	10.5 ± 1.4	12.3 ± 1.6	0.94 ± 0.18	$E2$	4
870.6 ± 0.2	$(25^+) \rightarrow 24^+$	2.9 ± 0.4	2.6 ± 0.4			Side
888.4 ± 0.1	$22^+ \rightarrow 20^+$	25.8 ± 2.0	27.3 ± 2.1	1.04 ± 0.16	$E2$	4
928.5 ± 0.2	$(28^+) \rightarrow 26^+$	7.5 ± 0.7	6.2 ± 0.6		$(E2)$	4
932.9 ± 0.5	$(27^+) \rightarrow (25^+)$	1.4 ± 0.3				Side
944.0 ± 0.3	$(29^+) \rightarrow (27^+)$	3.5 ± 0.5			$(E2)$	5
955.7 ± 0.3	$(31^+) \rightarrow (29^+)$	2.6 ± 0.5			$(E2)$	5
964.7 ± 0.2	$24^+ \rightarrow 22^+$	19.2 ± 2.9	18.9 ± 2.9	0.93 ± 0.13	$E2$	4
966.0 ± 0.3	$(25^+) \rightarrow 23^+$	11.4 ± 1.1	11.9 ± 1.2		$(E2)$	5
1017.4 ± 0.1	$12^+ \rightarrow 10^+$	100 ± 9			$E2$	
1020.7 ± 0.3	$(27^+) \rightarrow (25^+)$	7.9 ± 1.7	7.5 ± 1.6		$(E2)$	5
1035.4 ± 0.2	$14^+ \rightarrow 12^+$	27.0 ± 2.7		0.91 ± 0.15	$E2$	
1046.7 ± 0.5	$(34^+) \rightarrow (32^+)$	1.7 ± 0.3			$(E2)$	4
1056.8 ± 0.3	$16^+ \rightarrow 14^+$	6.5 ± 0.8		0.86 ± 0.23	$E2$	
1089.8 ± 0.2	$16^+ \rightarrow 14^+$	18.6 ± 1.9		0.98 ± 0.17	$E2$	
1096.6 ± 0.3	$(32^+) \rightarrow (30^+)$	2.4 ± 0.4			$(E2)$	4
1119.3 ± 0.2	$(30^+) \rightarrow (28^+)$	4.9 ± 0.7	3.1 ± 0.4		$(E2)$	4
1149.6 ± 0.5	$(29^+) \rightarrow (27^+)$	0.9 ± 0.4				Side
1161.5 ± 0.2	$14^+ \rightarrow 12^+$	26.3 ± 2.6		1.07 ± 0.18	$E2$	
1182.8 ± 0.3	$16^+ \rightarrow 14^+$	6.8 ± 0.8		1.12 ± 0.35	$E2$	
1215.9 ± 0.2	$16^+ \rightarrow 14^+$	13.4 ± 1.3		1.09 ± 0.24	$E2$	
1336.9 ± 0.4	$16^+ \rightarrow 14^+$	3.3 ± 0.7			$E2$	

[a] Intensities obtained for the ^{100}Mo(^{48}Ti,4n) reaction at 215 MeV.
[b] Intensities obtained for the ^{114}Cd(^{36}S,6n) reaction at 182 MeV.
[c] Adopted from ref. [8].

Table 2. Lifetimes and $B(E2, I \rightarrow I-2)$ values in the quadrupole bands 4 and 5 of ^{144}Gd. The uncertainties result from statistical contributions and from uncertainties related to the cascade- and side-feeding pattern.

Band	I^π	τ (ps)	$B(E2)$ (W.u.)	Applied analysis procedures[a]
4	20^+	0.56 ± 0.11	132^{+32}_{-22}	ng754 b; g1017 b, f
4	22^+	0.48 ± 0.09	68^{+16}_{-11}	ng888 b, f; g1017 b, f, sum
4	24^+	0.34 ± 0.07	64^{+17}_{-11}	ng965 sum; g754 b, f, sum, f-b
4	26^+	0.42 ± 0.09	105^{+29}_{-19}	g1017 + 754 f-b; g754 b, sum
4	28^+	0.47 ± 0.13	56^{+22}_{-12}	g1017 + 754 + 888 sum; g754 b
5	23^+	0.68 ± 0.11	76^{+15}_{-11}	g1017 b, f
5	25^+	0.37 ± 0.11	58^{+25}_{-13}	g793 b, f; g754 f-b

[a] The used abbreviations are explained in the text.

transition, de-exciting band 5 into band 4, reduced transition probabilities of $B(E1) = 5.3^{+2.3}_{-1.1} \cdot 10^{-4}$ W.u. and $B(M1) = 0.05^{+0.02}_{-0.01}$ W.u. are obtained. Although $E1$ transitions are often hindered, it is unlikely that the 465.7 keV transition has an $E1$ character because the hindrance would be quite large. However, the $B(M1)$ value is typical for transitions between signature partners. Therefore, a $M1$ character was assigned to it.

Furthermore, a weak structure de-exciting into the 24^+ level of band 4 has been observed.

The differences between the new level scheme and that previously published [8] result mainly from the fact that the $\approx$ 965 keV transition was found by the evaluation of γ-γ-γ coincidences to be a doublet consisting of the 964.7 and 966.0 keV lines. These transitions are not in coincidence with each other and hence have been placed in parallel into the new level scheme. The 966.0 keV transition is a member of the newly established quadrupole band 5. In band 4 the order of the 964.7 and 888.4 keV transitions has been exchanged with respect to the previous level scheme on the basis of intensity and lifetime arguments.

3.2 Lifetimes of quadrupole band levels in ^{144}Gd

3.2.1 Analysis of DSAM lineshapes

The analysis of experimental DSAM lineshapes was carried out using updated versions of the Monte Carlo codes COMPA, GAMMA and SHAPE [13,14]. The main features of the used approach are the following:

- *The kinematical spread of the recoils produced in the reaction is calculated on the basis of a statistical model taking into account step by step the evaporation of light particles from the compound nucleus.*
- *The slowing-down and multiple scattering of the recoils in the backed target can be calculated for several stopping layers using the special Monte Carlo approach discussed in appendix D.*
- *Any number of γ-ray detectors as well as their solid angles and geometrical arrangements can be defined.*
- *Side-feeding cascades from each entry state to each level of interest can be considered in the Monte Carlo simulation calculations (cf. appendix A). The number of levels and branches taken into account in the cascade feeding is not limited.*
- *Any condition of γ-γ coincidence gating ("up", "below", "narrow gate on transition below —NGTB", etc.) can be taken into account by the use of Monte Carlo techniques (cf. appendix B).*
- *Overlapping Doppler-broadened lines (up to seven in a multiplet in the present case) can be treated using the lifetimes as lineshape parameters.*

One of the features of this approach is its versatility, which has been achieved by the division of calculation and fitting procedures in three independent blocks. For compound nuclear reactions induced by charged particles, the distribution of the initial recoil velocities V_0 and their direction angles θ_0 with respect to the beam direction are calculated by the Monte Carlo code COMPA. The calculation starts with the simulation of the slowing-down of the projectiles of given bombarding energy in the target taking into account the dependence of the cross-section on the projectile energy. As a result, the velocity and position of the compound nucleus within the target are found for each event. Subsequently, the light-particle emission is simulated, taking into account the fission barrier and competition with statistical γ transitions. The output file of the code COMPA contains an array with the parameters of typically 100000 recoiling final nuclei before their slowing-down and γ-ray emission providing the high statistical accuracy of the calculations. The recoil parameters are the following: V_0 and θ_0 of each recoil, the geometrical position within the target as well as the excitation energy and angular momentum of the recoiling nucleus (entry state point).

In the second step of the calculation, the code GAMMA simulates for each event the slowing-down and multiple scattering of the recoils when they move through the target and stopper materials, the emission of γ cascades from the entry state point and the γ-ray absorption in the detectors by means of Monte Carlo methods utilizing the output of the code COMPA. The registration of γ-quanta is simulated simultaneously for all detectors (taking into account their sizes and geometries), positioned at different angles θ_j relative to the beam direction for twenty values of the lifetime τ_i of the nuclear levels (typically the lifetimes range from 0.01 to 10 ps in a logarithmic scale). In the present experiment using the γ-spectrometer GASP seven detector rings at the angles θ_1 to θ_7 are considered. The result of the simulation for each recoil history is a definite value of the relative Doppler shift $y = \Delta E_\gamma / E_\gamma$, which is stored in a spectrum of forty channels ranging from $y = -v_{0\max}/c$ to $y = +v_{0\max}/c$ for each pair of θ_j and τ_i values. In the calculations of these Doppler lineshapes not only side-feeding cascades from each entry state but also the cascade feeding along the known levels is taken into account. The software allows to take into account gates of any width placed on any transition of interest (cf. appendix B), as well as any coincidence condition for any γ-detector geometry, including a summation of all rings. In the most simple case of a gate on a transition below, *e.g.*, it is sufficient to accept the recoil histories of the events if the relative Doppler shifts of the recoils lie in a given interval which corresponds to the energy range of the gate. The results of the code GAMMA are stored in an output file containing 20 forty-channel spectra $I(y, \tau_i)$ for each detector ring at θ_j. This array allows for a lineshape analysis for any γ-ray energy as well as for any instrumental lineshape.

The code SHAPE is intended for the fit of DSAM lineshapes resulting from the experiment. The spectra $I(y, \tau_i)$ for each detector ring at θ_j, generated by the code GAMMA, are transformed into a set of 20 theoretical lineshapes $I(E_\gamma, \tau_i)$ for each value of θ_j. These lineshapes are calculated for the γ-ray energy E_γ of interest taking

into account the response function of the detector system (instrumental lineshape). In this way the theoretical Doppler lineshape for any value of τ can easily and very fast be determined by a simple interpolation procedure using the previously calculated spectra $I(E_\gamma, \tau_i)$. The lifetime value of the investigated level is found by a χ^2 fit of the experimental γ-ray lineshapes using the theoretical lineshapes. In case of a single peak, the code SHAPE performs a least-square fit with the lifetime, peak position and peak area as variable parameters. For two and more overlapping peaks, a simultaneous analysis is possible using lifetimes, positions and relative areas as parameters. Up to seven overlapping peaks can be fitted simultaneously which may have DSAM or instrumental lineshapes. For each γ-ray a separate set of input Doppler lineshapes has to be calculated with the code GAMMA. If a contamination line results from another reaction channel also the appropriate recoil kinematics and entry state population distribution has to be calculated with the code COMPA.

3.2.2 Results of lifetime analysis

The spectra for the lineshape analysis deduced from the γ-γ matrices for various detector angles are less clean than the γ-γ-γ coincidence spectra used for the level scheme analysis. Furthermore, the statistics from the GASP experiment is much smaller than that of the EUROBALL experiment. Hence, the lineshape analysis using the "gating above" technique [15,16], which would allow for a DSAM analysis free of the side-feeding problem, could not be applied for the high-spin states. Under these conditions the following procedures have been used:

1. Models to calculate time distributions of the side feeding with Monte Carlo methods have been developed and the relevant parameters were determined by the investigation of γ-ray multiplicity spectra for $^{142-146}$Gd and the lineshape of the 836.5 keV $26^+ \rightarrow 24^+$ transition of band 4 in ^{144}Gd [11] (cf. appendix A).
2. Special methods for the lineshape treatment have been developed and used. In particular for the transitions de-exciting the 28^+, 26^+ and 24^+ levels of band 4, spectra resulting from the summation over all 40 Ge detectors of the GASP spectrometer ("sum" spectra) have been used for the lineshape analysis. Because all detectors were summed, the resulting DSAM lineshapes are symmetric. For the 26^+ [11] and 24^+ levels difference spectra obtained by subtracting spectra of the backward detector ring from those of the corresponding forward detector ring ("f-b" spectra) have been analyzed. In this case the unshifted components of the line of interest as well as all unshifted background lines are removed and the resulting lineshape corresponds to an anti-symmetric reflection at a vertical line located at the unshifted γ-ray energy of the transition.
3. For the 24^+, 22^+ and 20^+ levels the "narrow gate on transition below" (NGTB) procedure [17] has been used in a generalized variant, which allows to place a gate of any position and width [18] (cf. appendix B). This method allows under particular conditions (especially if the effective lifetimes are small in comparison to the stopping times of the recoils) practically to bypass the side- and cascade-feeding problem and can, in spite of a fairly small sensitivity, be used to complement the "wide gate below" technique.

Lifetime values for each investigated level were obtained by carrying out two to five different lineshape analysis procedures. The "gate below" (g),"NGTB" (ng), "f-b" and "sum" methods have been applied. For the first three methods spectra have been produced for the backward (b) ring using the 144° and 148° detectors and the forward (f) ring using the 32° and 36° detectors. The instrumental lineshapes for these spectra were found to be the same in the present DSAM experiment using the GASP array. The results of the lifetime analysis are presented in table 2 and the applied methods and transitions used for gating are listed. The quoted uncertainties result from statistical contributions (given in the subsequent subsections) and from uncertainties related to the cascade- and side-feeding pattern. The statistical uncertainties are obtained by a χ^2 analysis [19] taking into account the variable parameters of all peaks in the fitted multiplet. Systematic errors arising from the uncertainties of the stopping power for the recoils ($\approx$ 10%, ref. [12]) are not included, since they influence all τ and $B(E2)$ values in the same way and the physical interpretation is only little affected. Intensities, important for taking into account cascade feeding, have been evaluated from the fit of the lineshapes together with the lifetimes in the "sum" spectra. Therefore, no corrections for angular correlation effects are required. The used intensities are included in table 1 as resulting from the ^{114}Cd(^{36}S,6n) reaction at 182 MeV. The intensities obtained from the thin-target experiment using the ^{100}Mo(^{48}Ti,4n) reaction at 215 MeV could not be used since the entry state population distributions are different for the two reactions, although the relative intensities obtained in the two experiments in general do not contradict each other. The parameters to simulate the side-feeding pattern, universal for all levels of interest, have been determined in ref. [11]. The corresponding time dependence of the side feeding was calculated for each level (cf. appendix A).

Detailed information on the lineshape analysis is given in the following subsections. Since the lineshape analysis was started at the top of the level scheme and step by step the lifetimes of the lower-lying levels were determined the presentation of the analysis is ordered correspondingly. For all subsequent figures displaying lineshape analysis results the sum of all fitted peaks as well as the fit for the line of interest are drawn as full curves. For a second line of interest in a multiplet the fit is drawn as dashed line and for contamination peaks the fits are drawn as dotted lines. Spectra resulting from matrices for individual-detector rings have an energy calibration of 1 keV per channel, whereas for sum spectra, resulting from the matrix containing events from all detectors, the energy calibration is 0.7 keV per channel.

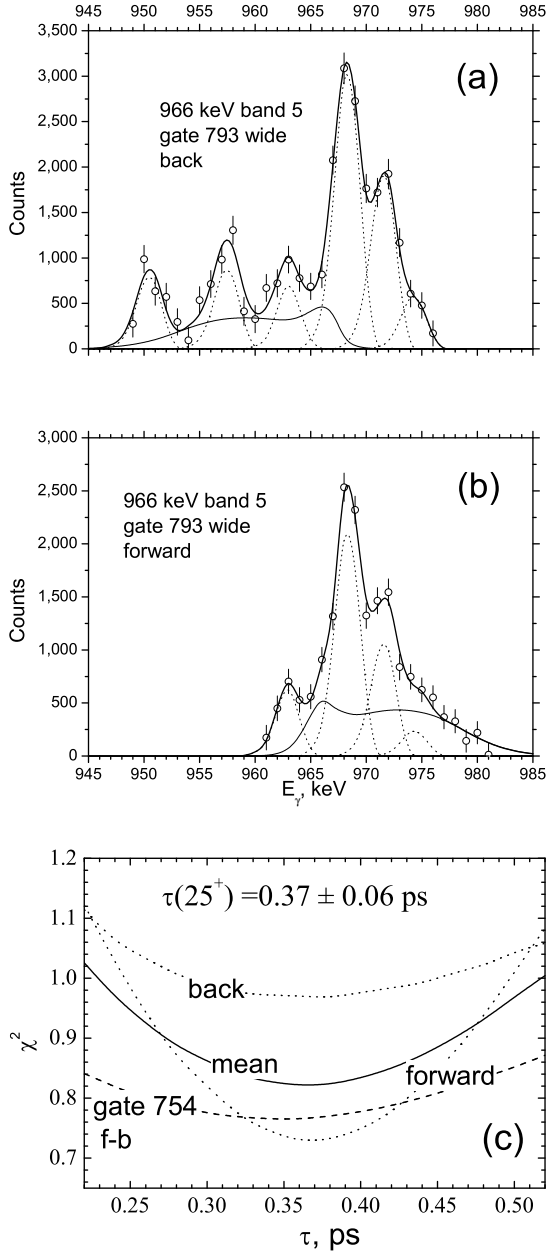

Fig. 3. (a), (b): results of the DSAM lineshape analysis for the 966.0 keV $25^+ \rightarrow 23^+$ transition. The energies of the contamination lines (dotted lines) have been found independently and were fixed in the fitting procedure. (c): χ^2 plots; the dashed line corresponds to a two-dimensional fitting of the "f-b" g754 spectrum, in which τ of the 24^+ level was varied (cf. fig. 4).

3.2.3 Lifetime analysis for the $I^\pi = 23^+, 25^+$ and $26^+, 28^+$ levels

The lifetime evaluation for the 28^+ and 25^+ levels in bands 4 and 5, respectively, suffers from problems related to the uncertainties in the cascade-feeding intensities. The feeding intensities from the respective preceding levels can only be evaluated very roughly due to the small statistics and the large Doppler broadening of the corresponding γ lines. The used intensities result from calculated side-feeding intensities (cf. ref. [11]). It has furthermore been assumed that the lifetimes of the 27^+ and 30^+ levels are ≈ 0.2 ps considering the observed dependence of the $B(E2)$ values on the spin.

Results of the DSAM lineshape analysis for the 966.0 keV $25^+ \rightarrow 23^+$ transition are presented in figs. 3a, b. The gate has been placed on the 792.7 keV transition de-exciting the 23^+ level to exclude the contribution of the more intense 964.7 keV $24^+ \rightarrow 22^+$ transition which shows a large Doppler effect (see below). Several contamination peaks with instrumental lineshapes obscure the lineshape of the 966.0 keV transition in forward and especially backward directions. The energy of this γ line has been determined in the thin-target experiment (cf. table 1) and has been fixed in the fitting procedure together with the energies of the contamination lines. The independent evaluation of the lifetime of the 25^+ state from gates, positioned below the 21^+ level is practically impossible except for the special case of the "f-b" method. In the corresponding normalized difference spectrum, shown in fig. 4c, gated on the 754.3 keV line, only the 964.7 and 966.0 keV components are present. Moreover, since the Doppler effect is for the 966.0 keV line larger than that of the 964.7 keV line (mainly due to the difference in the cascade feeding) and since the unshifted components are removed in the "f-b" spectrum, the contributions of the lineshapes of the 964.7 and 966.0 keV transitions turn out to be comparable (cf. fig. 4c) and a lifetime determination is possible for both. In the χ^2 diagram of fig. 3c the dashed line corresponds to the two-dimensional fit of the "f-b" g754 spectrum, for which τ of the 24^+ level was varied. The statistical error for the lifetime of the 25^+ level, obtained by considering all χ^2 curves is ± 0.06 ps.

A similar situation as described above exists for the 28^+, 26^+ and 23^+ levels. The statistical error of the lifetime of the 28^+ level is only ± 0.07 ps as compared to the value of ± 0.13 ps given in table 2. In case of the 836.5 keV transition de-exciting the 26^+ state a two-dimensional fit of the "f-b" spectrum gated on the 1017.4 and 754.3 keV lines, using the lifetime and the side-feeding intensity as fitting parameters, gave $\tau = 0.42 \pm 0.09$ ps. (cf. ref. [11]). The result of the analysis of the "sum" spectrum gated on the 754.3 keV line (cf. fig. 5a) is $\tau = 0.41 \pm 0.09$ ps and that for the "b" spectrum gated on the 754.3 keV line is $\tau = 0.43 \pm 0.11$ ps, the weighted average being $\tau = 0.42 \pm 0.06$ ps. In case of the 23^+ level the statistical error is ± 0.06 ps.

3.2.4 Lifetime analysis for the $I^\pi = 20^+, 22^+$ and 24^+ levels

In fig. 4 the DSAM lineshape analysis of the 964.7 keV $24^+ \rightarrow 22^+$ transition using the "wide gate below" technique is presented. All spectra were produced by gating on the 754.3 keV line. In portions (a) "forward" and (b) "backward" spectra are shown. The energy, lifetime and relative intensity of the 966.0 keV line (dashed line) as well as the energies of the contamination lines (dotted lines) have been determined independently and were fixed in

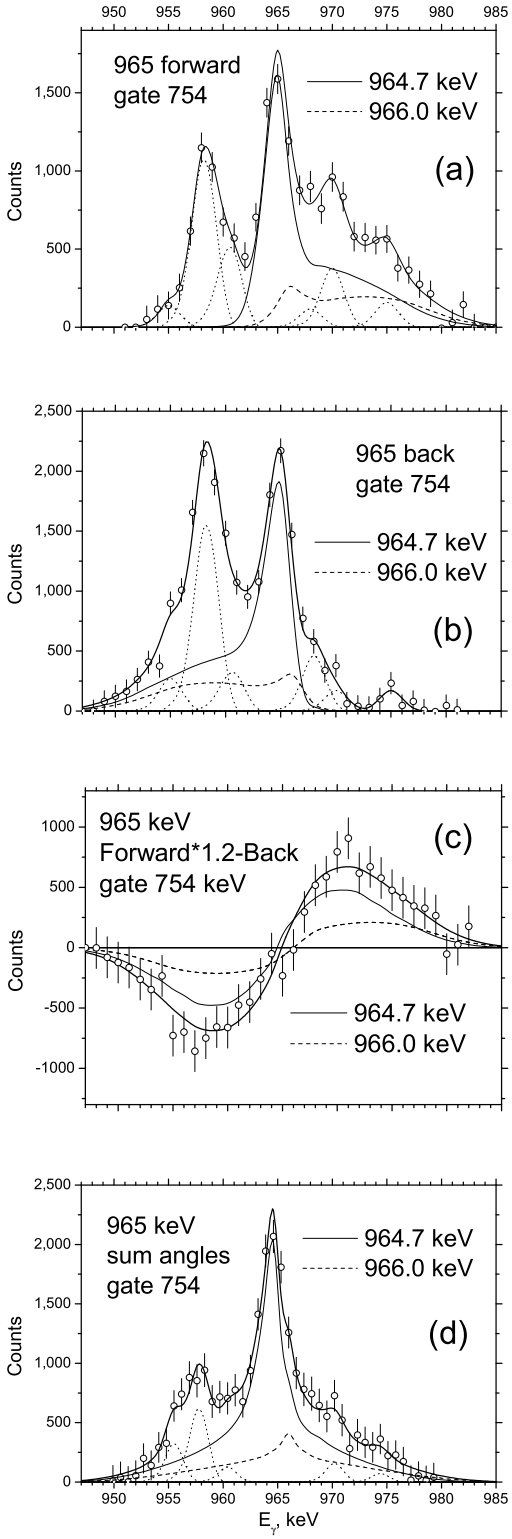

Fig. 4. DSAM lineshape analysis for the 964.7 keV $24^+ \rightarrow 22^+$ transition using the "wide gate below" technique. All spectra were produced by gating on the 754.3 keV line. (a), (b): "f" and "b" spectra. (c): normalized "f-b" spectrum. The full "f-b" curve through the data points represents a two-dimensional fit, when τ was varied for the 24^+ and 25^+ levels. (d): analysis of the "sum" spectrum.

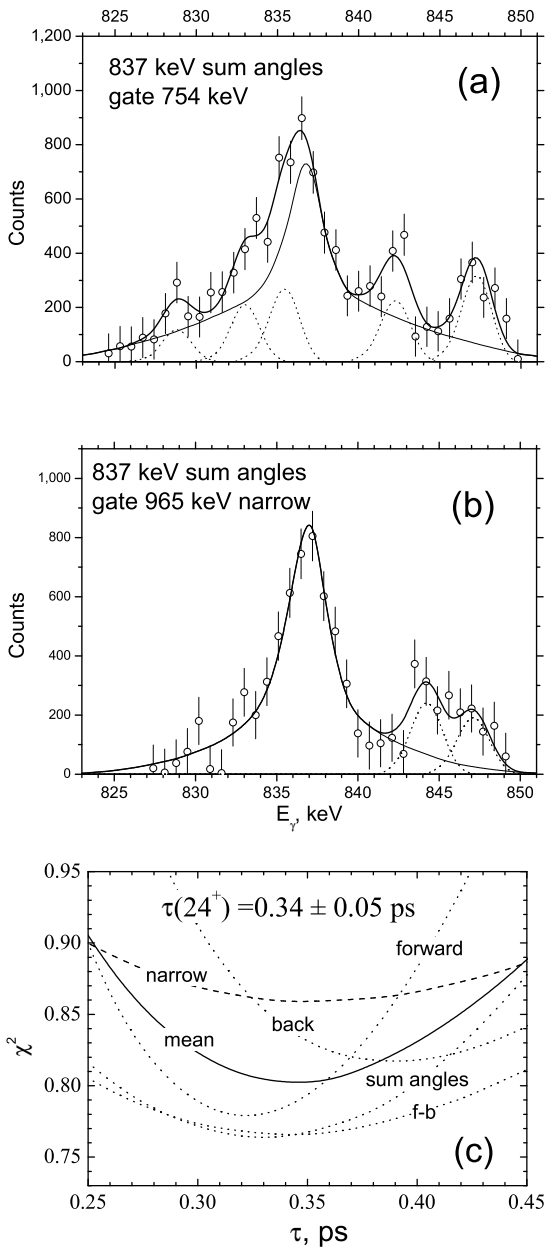

Fig. 5. DSAM lineshape analysis of the 836.5 keV $26^+ \rightarrow 24^+$ transition. (a): lineshape observed by setting a "wide gate below" on the 754.3 keV line. The solid lines correspond to a value of $\tau_{26^+} = 0.41$ ps. Positions of contamination lines (dotted lines) have been fixed in the fit. (b): the same as (a), but observed in a narrow gate below on the 964.7 keV line, corresponding to a lifetime $\tau_{24^+} = 0.35$ ps. (c): χ^2 plots; the dashed line corresponds to the NGTB fitting, whereas dotted lines are related to g754 spectra.

the fitting procedure. In portion (c) the normalized "f-b" spectrum is presented. The full "f-b" curve through the data points represents a two-dimensional fit, for which τ was varied for the 24^+ and 25^+ levels. An intensity ratio $I(966.0 \text{ keV})/I(964.7 \text{ keV}) = 0.36$ has been calculated for the spectrum obtained by gating on the 754.3 keV transition taking into account the branching ratios of the

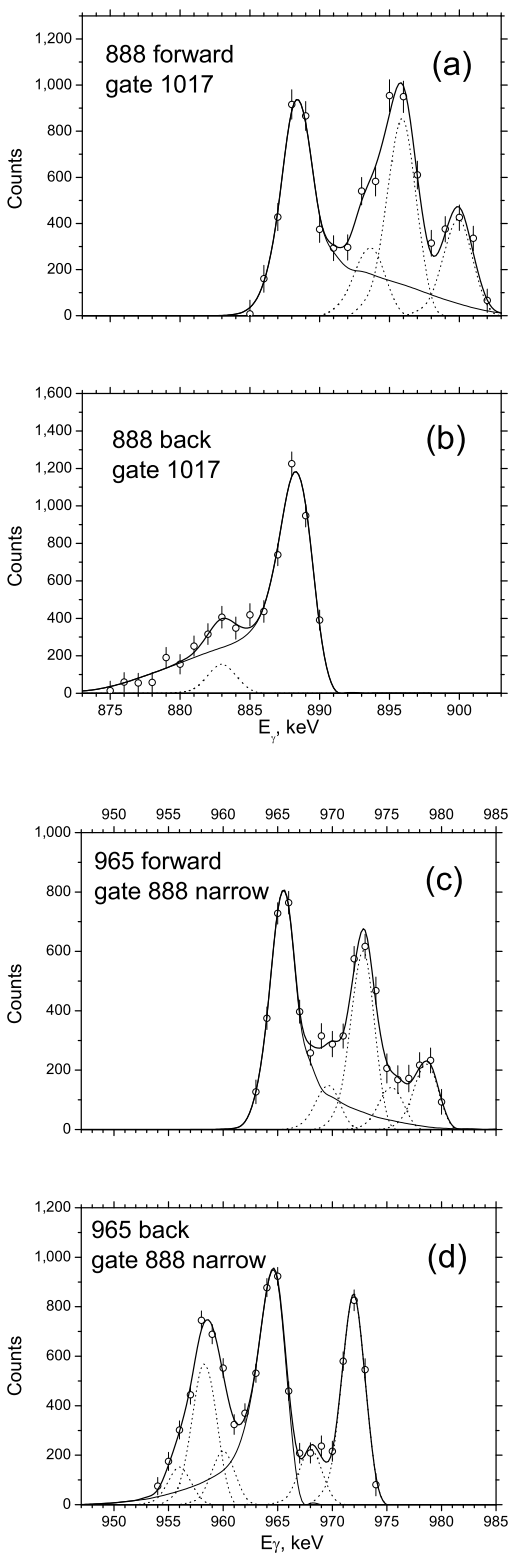

Fig. 6. DSAM lineshape analysis of the 888.4 keV $22^+ \rightarrow 20^+$ transition. (a), (b): "f" and "b" spectra, gated on the 1017.4 keV line. (c), (d): lineshapes of the 964.7 keV $24^+ \rightarrow 22^+$ transition, observed in narrow "f" and "b" gates on the 888.4 keV line. A small contribution due to the 966.0 keV $25^+ \rightarrow 23^+$ transition has been subtracted. Positions of contamination lines (dotted lines) have been fixed for the fit.

transitions de-exciting the 21^+ and 23^+ states and it was fixed in the fitting procedure. In portion (d) the analysis of the "sum" spectrum is presented.

For the 20^+, 22^+ and 24^+ levels a NGTB procedure [18] has been used in addition to the usual "gating from below" technique. In fig. 5 the application of the NGTB technique is illustrated for the 24^+ level based on the lineshape analysis of the 836.5 keV $26^+ \rightarrow 24^+$ transition. In portion (a) a "sum" spectrum obtained by setting a wide gate on the 754.3 keV transition located in the level scheme below the 836.5 keV transition is shown. The solid lines represent a fit for a lifetime value $\tau(26^+) = 0.41$ ps taking into account cascade and side feedings. The energies of the contamination lines (dotted lines) have been fixed during the fit. In portion (b) a "sum" spectrum is presented which was obtained by setting a narrow gate on the lower transition of 964.7 keV with a width of ± 2.5 keV as compared to the maximum Doppler shift of ± 25 keV (for details see appendix C). The full line represents a fit for a lifetime $\tau(24^+) = 0.35$ ps. The reduction of the Doppler effect is connected with the influence of the lifetime of the 24^+ level. In the χ^2 plots shown in portion (c) the dashed line corresponds to the NGTB fitting, whereas the dotted lines represent other analysis methods applied to spectra gated on the 754.3 keV line (cf. table 2). The full χ^2 curve represents the mean value of all methods used for the lifetime determination of the 24^+ level (cf. fig. 4).

In fig. 6 the DSAM lineshape analysis for the 888.4 keV $22^+ \rightarrow 20^+$ transition is presented. In portions (a), (b) "f" and "b" spectra, gated on the 1017.4 keV line are shown. In portions (c), (d) the lineshapes of the 964.7 keV $24^+ \rightarrow 22^+$ transition observed in narrow "f" and "b" gates on the 888.4 keV line are presented. A small contribution from the 966.0 keV $25^+ \rightarrow 23^+$ transition, arising from the weak 465.7 keV branch de-exciting the 23^+ level, has been subtracted. These spectra can be compared with spectra obtained by setting wide gates on the 754.3 keV line (cf. figs. 4a, b) and the reduction of the Doppler effect is obvious. The χ^2 analysis of the lineshape fits gives a lifetime $\tau(22^+) = 0.48 \pm 0.06$ ps.

In fig. 7 the DSAM lineshape analysis of the 754.3 keV $20^+ \rightarrow 18^+$ transition is shown. In the portions (a), (b) "f" and "b" spectra, gated on the 1017.4 keV line, are displayed. In portion (c) the lineshape of the 888.4 keV $22^+ \rightarrow 20^+$ transition, obtained by setting a narrow gate on the 754.3 keV line, is presented. The lineshape represents a reduction of the Doppler effect in comparison to that of the same transition, as obtained by gating on the 1017.4 keV line (cf. fig. 6b). In the χ^2 plots (fig. 7d) the dashed line corresponds to the NGTB fitting and the dotted lines represent the lineshape analysis using the spectra gated on the 1017.4 keV transition.

In all considered cases the results of the NGTB procedure are in excellent agreement with those obtained using the "wide gate below" technique. This fact indicates that the cascade and especially the side feedings have correctly been taken into account.

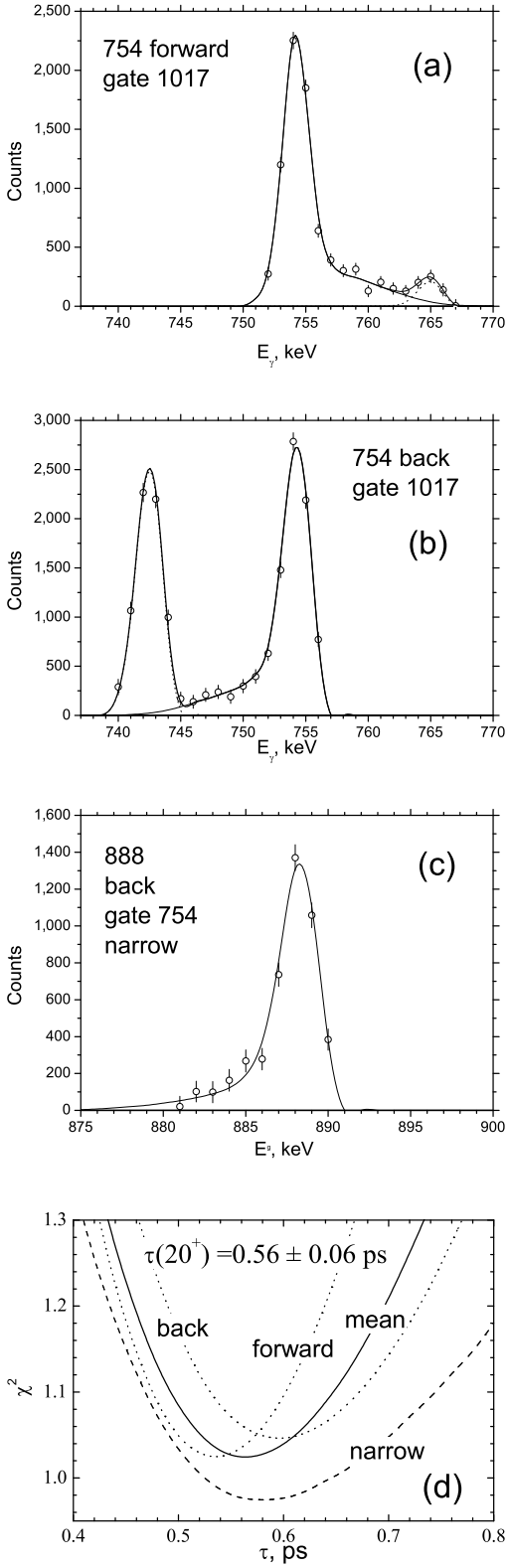

Fig. 7. DSAM lineshape analysis of the 754.3 keV $20^+ \rightarrow 18^+$ transition. (a), (b): "f" and "b" spectra, gated on the 1017.4 keV line. (c): lineshape of the 888.4 keV $22^+ \rightarrow 20^+$ transition, observed in a narrow gate on the 754.3 keV line. (d): χ^2 plots; the dashed line corresponds to the NGTB fitting and the dotted lines are related to the g1017 spectra.

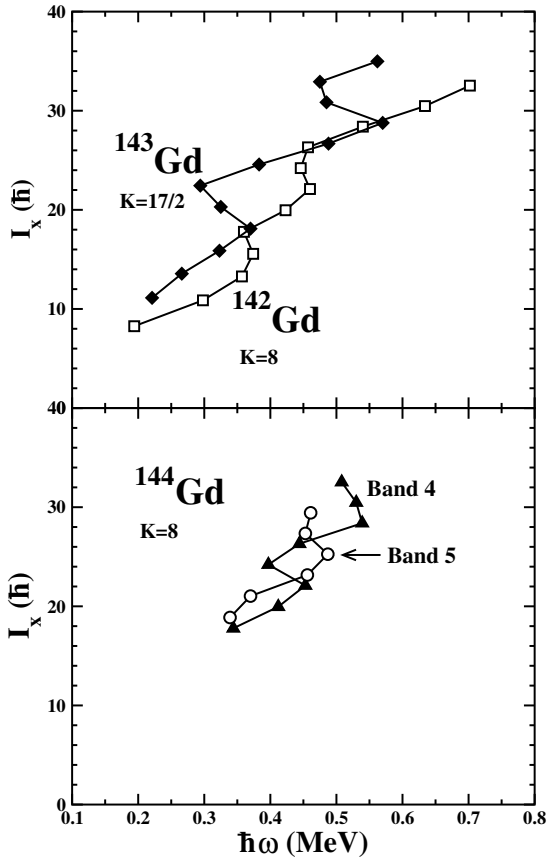

Fig. 8. Aligned angular momenta of the quadrupole bands 4 and 5 in ^{144}Gd (lower portion) and those of the quadrupole bands in ^{142,143}Gd (upper portion) *vs.* rotational frequency. In the calculation $K = 8$, 17/2 and 8 has been assumed for ^{142,143,144}Gd, respectively.

4 Discussion

In fig. 8 the aligned angular momenta of the quadrupole bands 4 and 5 in ^{144}Gd (lower portion) and those of the quadrupole bands in ^{142,143}Gd [3,4] (upper portion) are shown. These bands are considered to start at states with $I^\pi = 10^+$, $25/2^+$ and 18^+, respectively, for ^{142,143,144}Gd. In ^{142}Gd two coexisting 10^+ isomers [5], have been found having $(\pi h_{11/2})^2$ and $(\nu h_{11/2})^{-2}$ configurations, respectively, with collective structures built on them. The sequence based on the $(\pi h_{11/2})^2_{10^+}$ isomer has been extended to $I = 34$ [4] and its total aligned angular momentum has been included in fig. 8. The quadrupole band of ^{143}Gd has been established up to $I = 73/2$ and is considered to have a $(\pi h_{11/2})^2 \nu[400]1/2$ configuration [3]. Band 4 in ^{144}Gd develops above the $I^\pi = 18^+$ state. A $(\pi h_{11/2})^2 \otimes (\nu h_{11/2})^{-2}$ configuration may be assigned to band 4 (see below). To calculate the aligned angular momenta and rotational frequencies for the quadrupole bands in ^{142,143,144}Gd K values $K = 8$, 17/2 and 8 have been used, respectively. The K value of band 4 in ^{144}Gd will be discussed below. Band 4 in ^{144}Gd and the quadrupole bands in ^{142,143}Gd show a similar behaviour with two band crossings each at rotational frequencies $\hbar\omega \approx 0.37$

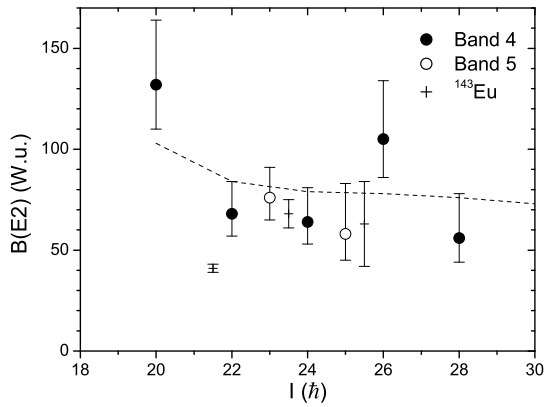

Fig. 9. Experimental $B(E2)$ values of bands 4, 5 in ^{144}Gd and the strechted $E2$ band in ^{143}Eu *vs.* angular momentum. The dashed line represents calculated $B(E2)$ values for band 4 (cf. sect. 4.1).

and $\approx$ 0.49 MeV, respectively. The corresponding alignment gains are $\approx$ 5.0 and $\approx$ 5.4$\hbar$. A quadrupole band with a similar alignment behaviour has also been observed in ^{143}Eu [20]. The band crossings may result from the breakup of $h_{9/2}$ and $i_{13/2}$ neutron pairs, respectively [3]. Since the strongly downsloping $i_{13/2}$ neutrons polarize the shape towards larger deformation, it is not easy to conclude whether first the alignment of the $i_{13/2}$ neutrons and subsequently that of the $h_{9/2}$ neutrons occur or vice versa. However, it is expected from the calculations presented in ref. [3], that for the long stretched $E2$ cascades in $^{142-144}$Gd the nuclear shape will move into a well-deformed, triaxial minimum ($\beta_2 = 0.25$, $\gamma = 26.5°$) at high spins. To prove this interpretation, lifetime information is required for the stretched $E2$ bands in $^{142-144}$Gd.

In fig. 9 the $B(E2)$ values for the bands 4 and 5 in ^{144}Gd are plotted as a function of the angular momentum. For comparison also $B(E2)$ values for the stretched $E2$ band of ^{143}Eu [20] are shown in fig. 9. It can be seen that they have the same magnitude as those of ^{144}Gd. The $B(E2)$ values for the bands in ^{144}Gd vary between $\approx$ 60 and 130 W.u. and show hence already for the low-spin members of these bands a considerable enhancement giving evidence for a significant nuclear deformation. The weighted-average $B(E2)$ value for band 4 in ^{144}Gd is 73 W.u. corresponding to $B(E2) = 0.33$ e^{2}b^2.

Total Routhian surface (TRS) calculations have been carried out to assign a configuration to band 4 in ^{144}Gd. As result, experimental and calculated excitation energies and total aligned angular momenta are compared for band 4 of ^{144}Gd in fig. 10 for the three lowest-lying configurations. The excitation energy is lowest for the curve with $\beta = 0.20$ and $\gamma = 17°$. The total aligned angular momentum is best reproduced by the curve for this configuration although it goes smoothly through the band crossings. The calculated total aligned angular momentum has to be understood as an average value, since many close lying band crossings exist which cannot be described by the cranking approximation. For the calculation of $B(E2)$ values of

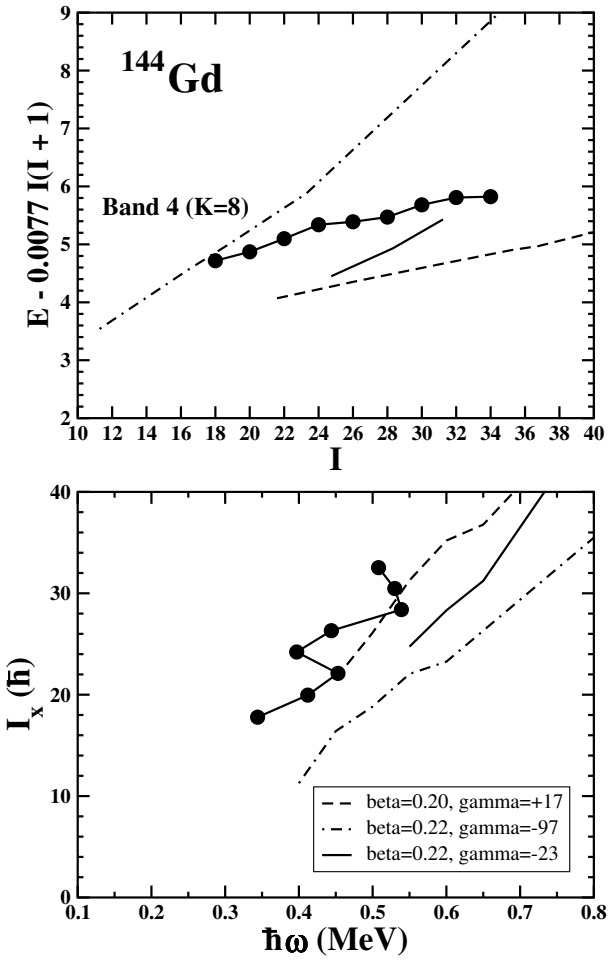

Fig. 10. Comparison of experimental and theoretical excitation energies (upper portion) and aligned angular momenta (lower portion) for the quadrupole band 4 in ^{144}Gd. The theoretical curves result from TRS calculations.

triaxial nuclei the following formula has been used [21]:

$$B(E2; I \to I \pm 2) = \frac{5}{16\pi} Q_2^2 \langle I\ K\ 2\ 0 | I-2\ K\rangle^2\ \text{e}^2\text{b}^2\,,$$

where

$$Q_2 = 0.0133\ ZA^{2/3}\beta\cos(\gamma+30)\ \ \text{eb}$$

for $r_0 = 1.2$ fm. The lowest-lying configuration has a $B(E2)$ value $B(E2) = 0.38$ e^{2}b^2 in very good agreement with the average experimental value for band 4. The calculated angular-momentum contributions are $I_\pi = 14$ and $I_\nu = 8$ for $I = 22$ indicating that a $(\pi h_{11/2})^2 \otimes (\nu h_{11/2})^{-2}$ configuration may be assigned to band 4. Since for an almost prolate shape the $(\pi h_{11/2})^2$ configuration has a vanishing K value, $K = 8$ may be assigned to band 4. The above configuration assignment is different from our previous $\pi h_{11/2}^2 \nu h_{11/2}^{-1} \nu h_{9/2}$ assignment with $\beta_2 = 0.22$ and $\gamma = -23°$ [8], however, this configuration has a $B(E2)$ value $B(E2) = 0.97$ e^{2}b^2 which is too large in comparison to the experimental result. The third low-lying configuration with $\beta_2 = 0.22$ and $\gamma = -97°$ has a $B(E2)$ value

$B(E2) = 0.15$ e^{2}b^2 considerably smaller than the experimental value.

Band 5 may be considered as the unfavoured sequence of band 4 since the aligned angular momenta and lifetimes of both bands are similar (cf. figs. 8 and 9).

4.1 Band 4 in ^{144}Gd and successive band crossings

The enhancement of the $B(E2)$ values in bands 4 and 5 points to the existence of a quadrupole collectivity in the states forming these bands. The experimental energies and $E2$ transition probabilities do not allow for an unambiguous conclusion as to whether the nucleus in these states is well deformed or soft with respect to deformations. On the one hand, the moments of inertia as calculated from energy differences according to the $I(I+1)/2\mathcal{J}$ law (I, $\mathcal{J}$ are the angular momentum and the moment of inertia, respectively) can be considered as an indirect argument for a deformation. The values of $\mathcal{J}$ are of the order of 50 MeV^{-1} comparable to the rigid-body moment of inertia for $A = 144$: $\mathcal{J}_{\text{r.b.}} \approx 56$ MeV^{-1}, being reasonable as at high angular momenta the pairing correlations disappear. On the other hand, the energy levels of these bands are almost equidistant and the $B(E2)$ values (60–130 W.u.) do not reach the values generic for well-deformed nuclei (~ 200 W.u.), *i.e.* these data serve as an argument against a strong deformation in these states.

Here an interpretation of the structure of these excitations is proposed assuming that they are generated by an interplay of excitations with definite angular momenta, and as such excitations the collective quadrupole d-bosons of IBM and high-spin quasiparticle excitations are employed. This approach is phenomenological and does not fix explicitly the quasiparticle structure of the states (which is superimposed on the collective excitations). However, taking into account that the heads of these bands possess high spins ($I \geq 18$), they have to involve not less than four quasiparticles.

Amongst all the multi-quasiparticle configurations with high spins there are sequences of states with small energy differences and similar internal structure. States of $(\pi h_{11/2})^2 \otimes (\nu h_{11/2})^{-2}$ configuration, mentioned above, and states involving the decoupling of a neutron $h_{9/2}$ pair can be considered as examples. Energy differences between states of such configurations are determined by interactions between quasiparticles in the same shell states and, therefore, they are much smaller than the differences between shells. The level energies depend on the proton and neutron spin, but to simplify the calculation the states with total quasiparticle spins $I_{\text{q}} = 18^+, 20^+, \ldots$ can be treated as equidistant with a constant energy difference $\delta\varepsilon$.

To allow for a superposition of collective and high-spin quasiparticle states we introduce a basis $|I_{\text{q}} I_{\text{c}} I\rangle$, where I_{q} and I_{c} are quasiparticle and collective angular momenta, respectively, and I is the total angular momentum of the state ($\boldsymbol{I} = \boldsymbol{I}_{\text{q}} + \boldsymbol{I}_{\text{c}}$). The collective angular momentum I_{c} is formed by d-bosons, the I_{c}-operator being $I_{\text{c}} = (d^+ d)^{(1)}/\sqrt{10}$. To find the wave functions requires the diagonalization of a model Hamiltonian, which comprises a collective Hamiltonian h_{c}, (its eigenfunction is $|I_{\text{c}}\rangle$), a quasiparticle one h_{q}, (its eigenfunction is $|I_{\text{q}}\rangle$) and interaction terms.

As a first attempt the Hamiltonian of the $SU(3)$-limit of IBM1 [22] has been taken and for h_{c} only the wave functions of the ground-state band are used ($|0^+\rangle$, $|2^+\rangle$, $\ldots, |10^+\rangle$). Therefore, h_{c} depends only on one parameter $\mathcal{J}_0$, the $SU(3)$ moment of inertia:

$$h_{\text{c}} = \frac{\boldsymbol{I}_{\text{c}}^2}{2\mathcal{J}_0}\,.$$

As mentioned above, the quasiparticle description has been simplified assuming that the excitation energy of the states increases with the spin I_{q}, *i.e.* the eigenvalues of h_{q} have the form

$$h_{\text{q}}|I_{\text{q}}\rangle = \left[\varepsilon + \frac{\delta\varepsilon}{2}(I_{\text{q}} - I_{\text{q}0})\right]|I_{\text{q}}\rangle,$$

where $I_{\text{q}0} = 18$ and ε and $\delta\varepsilon$ are parameters.

As interaction terms dipole-dipole (V_{D}) and quadrupole-quadrupole (V_{Q}) interactions are taken into account. The dipole-dipole interaction is

$$V_{\text{D}} = -\frac{1}{\mathcal{J}_{\text{C}}}(\boldsymbol{I}_{\text{q}} \cdot \boldsymbol{I}_{\text{c}})\,.$$

V_{D} is similar to the Coriolis term in the deformed nuclear Hamiltonian. Therefore the parameter $\mathcal{J}_{\text{C}}$ can be regarded as a moment of inertia. The term $(h_{\text{c}} + V_{\text{D}})$ is diagonal in this representation of the basis, hence for aligned ($I = I_{\text{q}} + I_{\text{c}}$) and anti-aligned ($I = I_{\text{q}} - I_{\text{c}}$) states one obtains

$$(h_{\text{c}} + V_{\text{D}})|I_{\text{q}},\ I_{\text{c}},\ I = I_{\text{q}} \pm I_{\text{c}}\rangle = \left\{\frac{I_{\text{c}}(I_{\text{c}}+1)}{2\mathcal{J}_0} \mp \frac{1}{\mathcal{J}_{\text{c}}}\begin{pmatrix} I_{\text{q}} I_{\text{c}} \\ I_{\text{q}} I_{\text{c}} + I_{\text{c}} \end{pmatrix}\right\}|I_{\text{q}},\ I_{\text{c}},\ I = I_{\text{q}} \pm I_{\text{c}}\rangle.$$

Thus, the important role of V_{D} consists in lifting the energies of anti-aligned states with spins $I < 18^+$ above the energies of the aligned ones ($I \geq 18^+$).

The quadrupole-quadrupole interaction V_{Q} is

$$V_{\text{Q}} = \kappa Q_{\text{q}} \cdot Q_{\text{c}}$$

providing the coupling between configurations with different values of I_{q} and I_{c}, *i.e.* the diagonalization of the total Hamiltonian is reduced to a diagonalization of V_{Q}. Q_{c} is a quadrupole operator in the $SU(3)$-limit of IBM

$$Q_{\text{c}} = d^+ s + s^+ d - \frac{\sqrt{7}}{2}(d^+ d)^{(2)}$$

and Q_{q} is a standard quadrupole operator in the quasipartical space. Matrix elements of V_{Q} are factorized in the form

$$\langle I'_{\text{q}} I'_{\text{c}} I|\kappa Q_{\text{q}} \cdot Q_{\text{c}}|I_{\text{q}} I_{\text{c}} I\rangle = (-1)^{I+I'c+Iq} \begin{Bmatrix} I & I'_{\text{c}} & I'_{\text{q}} \\ 2 & I_{\text{q}} & I_{\text{c}} \end{Bmatrix} \times \kappa \langle I'_{\text{q}}||Q_{\text{q}}||I_{\text{q}}\rangle \langle I'_{\text{c}}||Q_{\text{c}}||I_{\text{c}}\rangle.$$

Table 3. Amplitudes of the main components of the wave functions for band 4. The following parameters have been used in the calculation: $\varepsilon = 7.45$ MeV, $\delta\varepsilon = 1.0$ MeV, $J_0 = 1.7$ MeV^{-1}, $J_C = 68$ MeV^{-1}, $t = 0.3$ MeV, $e^* = 12.53$ e $\cdot$ fm^2.

I^π	Wave function amplitudes			
18^+	$0.98(18_q0_c)$	$-0.17(18_q2_c)$	$-0.11(20_q2_c)$	
20^+	$0.65(18_q2_c)$	$-0.73(20_q0_c)$	$0.17(20_q2_c)$	
22^+	$0.70(20_q2_c)$	$-0.68(22_q0_c)$	$0.16(22_q2_c)$	
24^+	$0.73(22_q2_c)$	$-0.65(24_q0_c)$	$0.15(24_q2_c)$	
26^+	$0.76(24_q2_c)$	$-0.62(26_q0_c)$	$0.14(26_q2_c)$	
28^+	$0.79(26_q2_c)$	$-0.58(28_q0_c)$	$0.13(28_q2_c)$	
30^+	$-0.10(26_q4_c)$	$0.82(28_q2_c)$	$-0.55(30_q0_c)$	$0.12(30_q2_c)$
32^+	$-0.10(28_q4_c)$	$0.85(30_q2_c)$	$-0.51(32_q0_c)$	$0.12(32_q2_c)$
34^+	$-0.11(30_q4_c)$	$0.88(32_q2_c)$	$-0.46(34_q0_c)$	$0.10(34_q2_c)$

The reduced matrix element $\langle I'_c||Q_c||I_c\rangle$ is calculated with $SU(3)$ wave functions of IBM and the matrix element $\langle I'_q||Q_q||I_q\rangle$ depends on the structure of the quasiparticle states. Since a phenomenological aproach is used the detailed structure of the states is disregarded and a new parameter t is introduced:

$$t = \kappa(\langle I'_q||Q_q||I_q\rangle)_{\text{averaged}}.$$

Thus, the theoretical energies of the states under consideration are determined in this approach by 5 parameters: $\mathcal{J}_0$, ε, $\delta\varepsilon$, $\mathcal{J}_C$, t. To find theoretical $B(E2)$ values, wave functions have to be calculated, which are superpositions of the basic functions

$$|\Psi^I\rangle = \sum_{I_qI_c} \alpha^{(I)}_{I_qI_c}|I_qI_cI\rangle,$$

$\alpha^{(I)}_{I_qI_c}$ being amplitudes. They are used to calculate matrix elements of the $E2$ transition operator $T(E2)$. Here only the collective part of the $E2$ operator is taken into account assuming that the quasiparticle part is small in comparison with the collective one. In this approximation the $E2$ operator is proportional to Q_c:

$$T(E2) = e^*Q_c\,.$$

Thus the set of fitted parameters is supplemented by one more parameter e^*, the effective charge, giving 6 parameters. The value of e^* used in table 3 is chosen so that the $B(E2)$ values for band 4 are reproduced on average for a total number of IBM s- and d-bosons equal to 10. This number is somewhat larger than the canonical value (half of the valence nucleon number), since high-energy excitations are considered.

To describe the large $B(E2)$ values for the $20^+ \to 18^+$ transition and the subsequent decrease of $B(E2)$ it is assumed (and parameters are fitted in such a way) that each state with spin I, excluding the band head ($I = I_q = 18^+$), consists of two almost equal components with $I_q = I - 2$ and $I_q = I$. In other words, before a rotational band on each state with $I_q = I$ can start to develop, a band crossing occurs and in a state with $I + 2$ appears a component with $I'_q = I + 2$. The main components of the wave functions are given in table 3. Such a mechanism, which can be called a successive band crossing, permits to account for the lowering of the $B(E2)$ values (from ≈ 100 to 70 W.u.) and to reproduce the excitation energies of the band 4 states as can be seen in table 4. The mean deviations in the energies are 0.1 MeV. In the suggested approach the second theoretical energy eigenvalues ($E(I_2)$) for each spin I are found to be close to the first eigenvalues for the states with $I + 2$: $E(I_2) \lesssim E((I + 2)_1)$, except for $E(18_2) = 9.5$ MeV which is much larger than $E(20_1) = 8.1$ MeV. Therefore the intensities of the $(I + 2)_1 \to I_2$ transitions have to be much smaller than those for the $(I + 2)_1 \to I_1$ transitions and so such states (I_2) are not excited by transitions from band 4. The calculated $B(E2)$ values for band 4 are compared in table 4 and fig. 9 with the experimental ones.

Table 4. Comparison between the experimental and calculated excitation energies and $B(E2)$ values for band 4 in ^{144}Gd. The same parameters as given in the caption of table 3 have been used.

I^π	E (MeV)		$I^\pi_i \to I^\pi_f$	$B(E2)$ (W.u.)	
	Exp.	Th.		Exp.	Th.
18^+	7.351	7.35			
20^+	8.105	8.06	$20^+ \to 18^+$	132^{+32}_{-22}	103
22^+	8.994	9.04	$22^+ \to 20^+$	68^{+16}_{-11}	84
24^+	9.958	10.03	$24^+ \to 22^+$	64^{+17}_{-11}	79
26^+	10.795	11.02	$26^+ \to 24^+$	105^{+29}_{-19}	78
28^+	11.723	12.00	$28^+ \to 26^+$	56^{+22}_{-12}	76
30^+	12.842	12.98	$30^+ \to 28^+$		73
32^+	13.939	13.95	$32^+ \to 30^+$		69
34^+	14.986	14.92	$34^+ \to 32^+$		66

The present explanation of energies and $B(E2)$ values in band 4 should be considered as qualitative, since 6 parameters have been used to describe 14 empirical values of energies and transition probabilities. Band 5 can be described in the same way. It is believed that a more microscopical approach including calculations of quasiparticle configurations, their energies and the effective interactions between quasiparticles and bosons could decrease the amount of fitted parameters. However, the results of the present phenomenological analysis can be useful for such microscopical calculations, since a new mechanism

is suggested, *viz* that quasirotational bands with strong $E2$ transitions are formed through the mixing of various quasiparticle configurations interacting with collective excitations.

5 Conclusions

For a level scheme investigation of ^{144}Gd experimental data obtained with the γ-spectrometer EUROBALL III have been used. The high-spin states were populated by means of the ^{100}Mo(^{48}Ti,4n) reaction at 215 MeV. The known quadrupole band 4 has been modified and a new quadrupole band 5 was established. Lifetimes have been measured with the γ-spectrometer GASP using the Doppler-shift attenuation method. The ^{114}Cd(^{36}S,6n) reaction at $E = 182$ MeV was used in this experiment. Reduced transition probabilities $B(E2)$ were determined for seven members of the quadrupole bands 4 and 5. They show values between ≈ 60 and 130 W.u. and this considerable enhancement gives evidence for a significant nuclear deformation. A $(\pi h_{11/2})^2 \otimes (\nu h_{11/2})^{-2}$ configuration may be assigned to the quadrupole band 4 according to total Routhian surface calculations with deformation parameters $\beta = 0.20$ and $\gamma = 17°$. The spin dependence of the $B(E2)$ values has been explained by calculations using the collective quadrupole d-bosons of IBM and high-spin quasiparticle excitations. On the basis of these calculations a new mechanism is suggested, *viz* that quasirotational bands with strong $E2$ transitions are formed through the mixing of quasiparticle configurations interacting with collective excitations. This effect has been called a successive band crossing.

We are grateful to I. Hamamoto for some useful advice. We are indebted to the technical staff of the tandem XTU and ALPI accelerator combination of the Laboratori Nazionali di Legnaro for providing the beam. The work was in part funded by IB of BMBF at DLR, Germany, under the German-Russian WTZ contract RUS 99/191, by the EU under the contract ERBCHRXCT930364 and by the Volkswagen Foundation under contract number I/71 976.

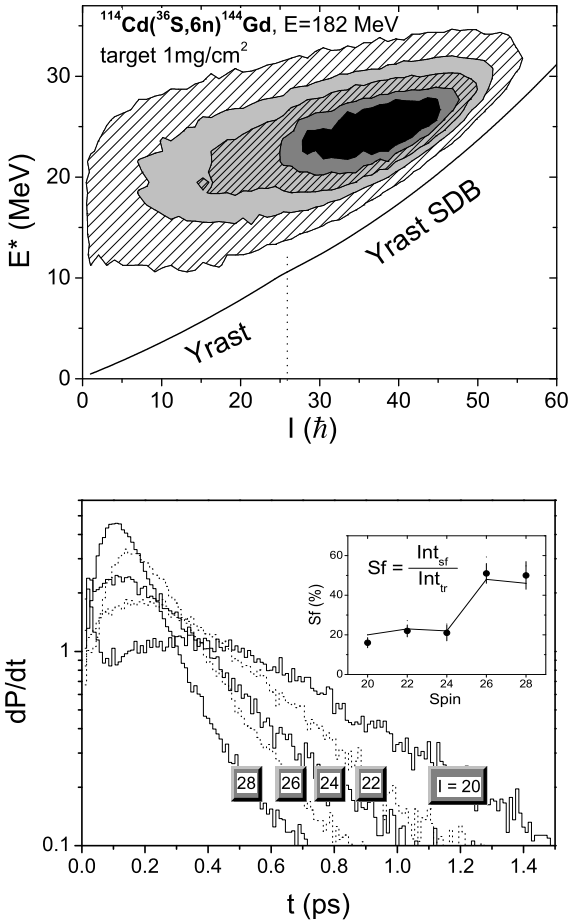

Fig. 11. Upper portion: entry state population distribution for ^{144}Gd, populated in the ^{114}Cd(^{36}S,6n) reaction at $E = 182$ MeV. Lower portion: Monte Carlo simulations of side-feeding time distributions dP/dt for the 20^+ to 28^+ members of band 4 in ^{144}Gd. The calculations have been performed for all levels with the same set of parameters to describe the de-excitation of the entry states to the states of interest. In the inset experimental and calculated (solid line) relative side-feeding intensities are presented.

Appendix A. Side-feeding time distributions in the ^{114}Cd(^{36}S,6n)^{144}Gd reaction at E = 182 MeV

The side-feeding time distributions dP/dt for the population of discrete states depends on the location of the entry state population distribution with respect to those of the levels of interest. The entry state population distribution for ^{144}Gd, populated in the ^{114}Cd(^{36}S,6n) reaction at $E = 182$ MeV is shown in the upper portion of fig. 11. It has been obtained by a Monte Carlo simulation of 10^6 events with the code COMPA, taking into account the slowing-down of the projectiles in the 1 mg/cm^2 thick target. The location of the entry states depends particularly on the competition between fission and neutron evaporation. The parameters for the description of the fission barrier have been deduced in an investigation of γ-ray multiplicity distributions measured for various reactions populating the nuclei $^{142-146}$Gd [11,23]. The side-feeding cascades between the entry states and the considered levels have been simulated with the program GAMMA. In the de-excitation of the entry states statistical $E1$, $M1$ and $E2$ transitions and stretched $E2$ bands with rotational damping have been taken into account. Because the considered nuclei are situated close to the semi doubly magic nucleus ^{146}Gd, furthermore, the influence of superdeformed bands and the existence of a large amount of particle-hole excitations in the entry state region, which generate bands of magnetic dipole transitions, are considered. The relative densities of the magnetic dipole and superdeformed bands

have been taken from the investigation of the multiplicity distributions and from the DSAM lineshape analysis of the 837 keV $26^+ \rightarrow 24^+$ transition in band 4 of ^{144}Gd, which is $\approx 50\%$ populated by side feeding [11]. Results of Monte Carlo simulations for the side-feeding time distributions $\mathrm{d}P/\mathrm{d}t$ for the 20^+ to 28^+ members of band 4 in ^{144}Gd are presented in the lower portion of fig. 11. All simulations have been performed with the same set of parameters. In the inset experimental and calculated relative side-feeding intensities are presented. The increase of the side-feeding intensity at $I = 26$ results from the fact that the crossing of the normal and superdeformed yrast lines occurs near this spin value. The good description of the side-feeding intensities and the fact that the Doppler lineshape analysis gives the same lifetimes when the NGTB (narrow gate on transition below) and WGTB (wide gate on transition below) methods are applied, indicate that the side-feeding time distributions are described with sufficient accuracy by the Monte Carlo simulation calculations.

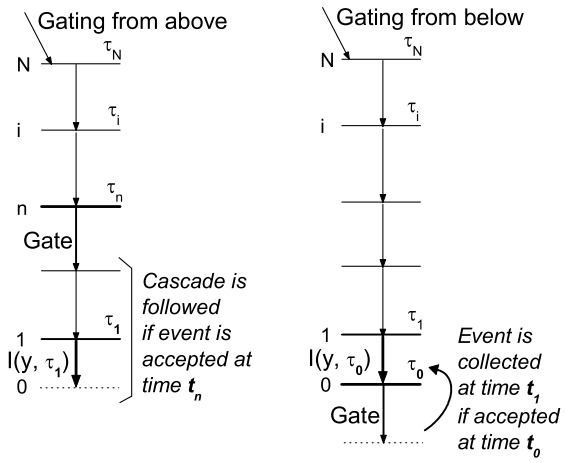

Fig. 12. Schematic depicture of the level schemes used in the Monte Carlo simulation calculations for the GTA (gating on a transition above) and NGTB (narrow gate on transition below) methods.

Appendix B. Monte Carlo simulation of gating

Generally lineshapes are calculated using an exponential decay law $\mathrm{d}P/\mathrm{d}t = \tau^{-1}\, e^{-t/\tau}$ and, if no gating condition is imposed, cascade feeding can be taken into account by a superposition of lineshapes corresponding to the exponential decay law of each level. This approach has, *e.g.*, been used in refs. [14,19]. In the framework of this scheme it is difficult to take into account gating conditions because they change the correlation between the velocity of the recoil and the time at which the γ-ray of interest is emitted. One way to include gating conditions into the lineshape analysis is to consider the integral convolution of the time-velocity probability functions for the cascade transitions [15,24].

By the use of Monte Carlo methods, as in the new version of the code GAMMA used in the present work, a simple description is obtained since each cascade is simulated and the time is considered as a random number. For the time at which the gating transition is emitted, obtained by summing the times of the cascade transitions, the velocity and the direction of the recoil are simulated. This information is used to calculate the γ-ray energy of the gating transition in a given detector. Subsequently it is checked whether the gating condition is fulfilled taking into account the instrumental lineshape.

For this purpose the γ-ray energy is converted into a channel number $E_\gamma \sim N_{\mathrm{ch}}$ using

$$N_{\mathrm{ch}} = N_{\mathrm{ch}_0}(1 + \cos(\vartheta_{v,\gamma})\, v(t_n)/c) + \Delta N_{\mathrm{random}},$$

where $v(t_n)$ is the recoil velocity at the time of detection t_n of the γ-ray in the detector, $\vartheta_{v,\gamma}$ the angle between the flight direction of the recoil and the point at which the γ-ray hits the detector and N_{ch_0} is the unshifted position of the γ line. The quantity $\Delta N_{\mathrm{random}}$ is used to describe the influence of the instrumental lineshape and is simulated as $\Delta N_{\mathrm{random}} = \sigma_{\mathrm{ap}}\, \xi$, where $\sigma_{\mathrm{ap}} = \mathrm{FWHM}/2.3548$ is the width assuming a Gaussian instrumental lineshape and ξ is a Gaussian-distributed random number. Assuming a gate interval of N_{L} – N_{R} then an event is accepted if $N_{\mathrm{L}} \leq N_{\mathrm{ch}} \leq N_{\mathrm{R}}$.

The further treatment of the accepted events depends on the applied gating method. The logical scheme for gating on a transition above the transition of interest (GTA method) is illustrated in the left portion of fig. 12 The level of interest is labelled as 1 and the array $I(y, \tau_1)$ (cf. sect. 3.2.1) is calculated with GAMMA for the transition $1 \rightarrow 0$. The level depopulated by the gating transition is numbered n and the highest-lying level in the cascade has the number N, being equal to the number of levels in the considered path. The side-feeding cascade reaches this level at the time t_{sf}. The simulated time at which a γ-quantum de-excites the level n is $t_n = t_{\mathrm{sf}} + \sum_{i=n}^{N} t_i$, where $t_i = \tau_i\ \ln(1/\zeta)$, ζ being an evenly distributed random number in the interval $\zeta \in (0, 1)$. For the event accepted at the time t_n the cascade is followed until the time at which a γ-quantum de-excites the level of interest $t_1 = t_n + \sum_{i=2}^{n-1} t_i + \tau_1\ \ln(1/\zeta)$ and the corresponding relative Doppler shift $y = \cos(\vartheta_{v,\gamma})\, v(t_1)/c$ is collected in the array $I(y, \tau_1)$ for 20 standard values of τ_1.

If a wide gate on a transition below the transition of interest is set (WGTB method) then the same procedure as above is used but no gate condition is set so that all events are accepted. The conditions for a wide gate are: i) if a Doppler effect exists then the gate width must be equal to the full width of the lineshape and ii) if the lifetime is much larger than the stopping time then all events correspond to the stopped component and the gate can have any width. The realization of the narrow gate on transition below (NGTB) technique [17] is shown in the right portion of fig. 12. The procedure is similar to the

GTA method but for an event for which the gate condition is fulfilled the time is calculated as $t_0 = t_1 + \tau_0 \ln(1/\zeta)$, where $t_1 = t_{\rm sf} + \sum_{i=1}^{N} t_i$ and for the lifetime τ_0 of the level de-excited by the gating transition 20 standard values are used. Thus in this case the array $I(y, \tau_0)$ is calculated for the transition $1 \rightarrow 0$ using the lifetime of the level de-excited by the gating transition below and after the fit of the lineshape for the $1 \rightarrow 0$ transition the lifetime of the level below is obtained. The event is collected at the time t_1 if it has been accepted at the time t_0.

Appendix C. Sensitivity of the NGTB method

In the NGTB (narrow gate on transition below) method ideally only the stopped component of the transition below should be selected for gating, but in practice this condition is difficult to realize, especially if spectra summed over all detector angles are treated. An increase of the gate width is useful and important to increase the statistical accuracy but it generally results in a decrease of the sensitivity with respect to the lifetime evaluation. In fig. 13 the sensitivity of the NGTB method is illustrated for the 837 keV $26^+ \rightarrow 24^+$ transition of band 4 in ^{144}Gd if gates of various widths are set on the 965 keV $24^+ \rightarrow 22^+$ transition. If individual-detector rings are used, the slope of the relative Doppler shift $F(\tau) = \frac{\langle \Delta E\gamma \rangle}{\langle \Delta E\gamma \rangle_{\rm max}}$ as a function of the lifetime τ of the level de-excited by the gating transition can be used as a measure of the sensitivity. If 90° detectors or sums of symmetrical detector rings, particularly sums of all rings, are used to increase the statistical accuracy, then $F(\tau) = 0$ and it cannot be used anymore as a measure of the sensitivity. In this case the slope of the relative width of the Doppler lineshape can be used as a measure of the sensitivity. It is defined as $W(\tau) = \frac{\sqrt{D_\gamma}}{\langle \Delta E\gamma \rangle_{\rm max}}$, where D_γ is the dispersion of the lineshape. The dashed lines in fig. 13 correspond to the limiting cases of using a wide gate and an infinitely narrow gate, respectively. The solid lines correspond to the experimental conditions used in the analysis with a gate width of 1378 ± 3 channels (965 ± 2.5 keV). The gate width is about 2 · FWHM and changes the sensitivity of the NGTB analysis only little with respect to the ideal case since the lifetime of 0.34 ps of the 24^+lower level lies in the optimal range of lifetimes.

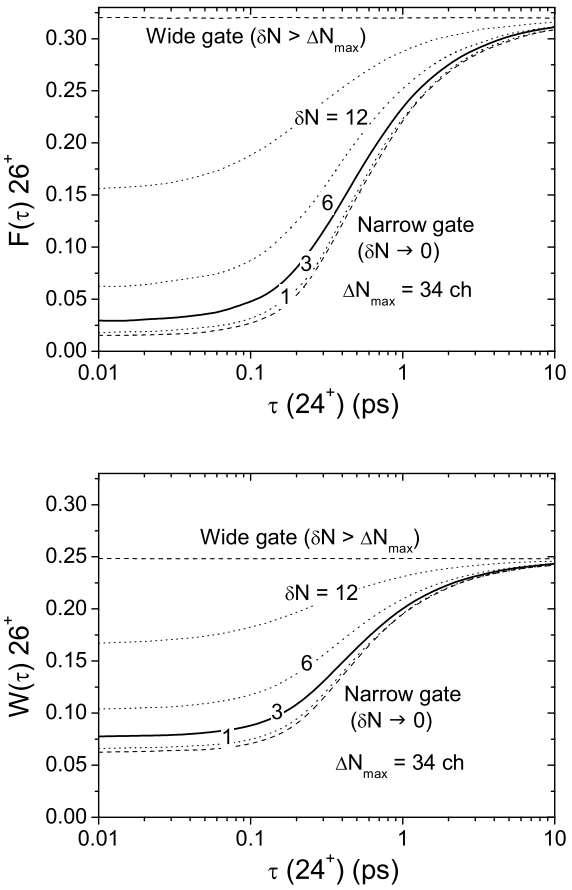

Fig. 13. Sensitivity of the NGTB (narrow gate on transition below) method for the 837 keV $26^+ \rightarrow 24^+$ transition of band 4 in ^{144}Gd if gates of various widths are set on the 965 keV $24^+ \rightarrow 22^+$ transition. The slopes of the $F(\tau)$ (upper portion) and the $W(\tau)$ (lower portion) curves are measures of the sensitivity. Dashed lines represent the limiting cases of using a wide gate and an infinitely narrow gate, respectively. The solid lines represent the experimental conditions with a gate width of three channels. The dotted lines are calculated for other gate widths.

Appendix D. Recoil velocity distribution at the time of γ-ray emission

To calculate the velocity and direction of a recoil at the time t_1 at which the γ-ray of interest is emitted, the slowing-down and multiple scattering of the recoils in the target-stopper combination is simulated with the program GAMMA. In the present experiment the ^{114}Cd target was backed by two layers of stopper materials, *viz* Ta and Bi (cf. sect. 2) as depicted in the left portion of fig. 14. The recoiling final nucleus is produced at the position (depth) R_0 in the target and is flying with an initial velocity V_0 under an angle θ_0 with respect to the beam direction. Initially, the recoil time $t(V)$ along the track and the projected range $R_{\rm pr}(V)$ are calculated as a function of the recoil velocity V for the target material, as illustrated in the right portion of fig. 14:

$$t(V) = m \int_0^V \left[\frac{{\rm d}E}{{\rm d}x}(V) \right]^{-1} {\rm d}\,V$$

and

$$R_{\rm pr}(V) = m \int_0^V V \overline{\cos\phi}(V) \left[\frac{{\rm d}E}{{\rm d}x}(V) \right]^{-1} {\rm d}\,V\,,$$

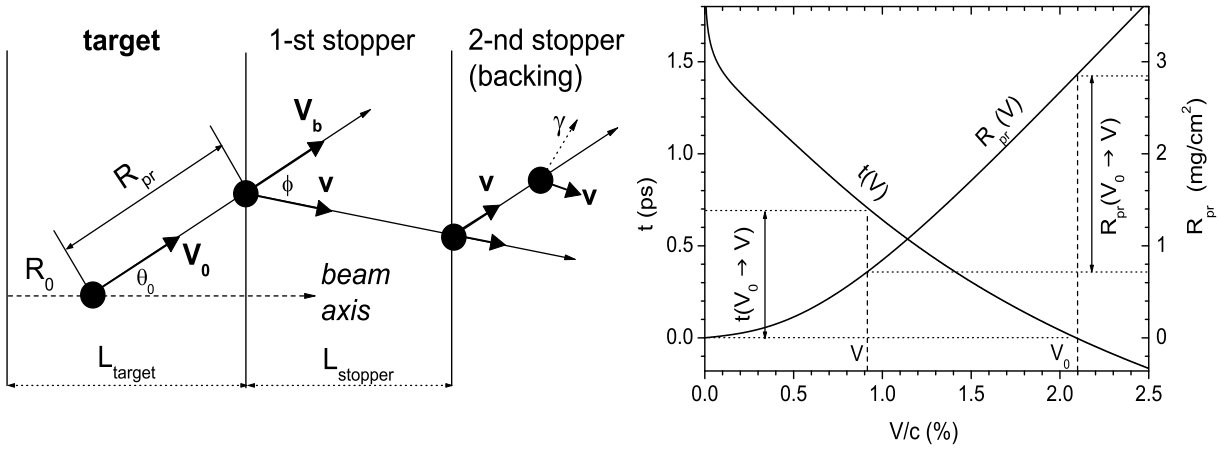

Fig. 14. Left portion: schematic diagram of the scattering process for a target backed by two stopping materials. Right portion: recoil time along the track (left-hand scale) and projected range (right-hand scale) as a function of the recoil velocity V for the target material. For the time of the γ-ray emission $t(V_0 \to V)$ the velocity V and the projected range $R_{\rm pr}(V_0 \to V)$ can be extracted.

where $\frac{{\rm d}E}{{\rm d}x}(V)$ is the recoil stopping power, being the sum of electronic and nuclear components:

$$\frac{{\rm d}E}{{\rm d}x}(V) = \left[\frac{{\rm d}E}{{\rm d}x}(V)\right]_{\rm e} + \left[\frac{{\rm d}E}{{\rm d}x}(V)\right]_{\rm n}$$

and $\overline{\cos\phi}(V)$ is the mean value of the cosine of the multiple-scattering angle ϕ.

The time $t_1 = t(V) - t(V_0)$ is used to extract the recoil velocity V at the time of γ-ray emission and with this information the corresponding projected recoil range $R_{\rm pr}(V_0, V)$ is deduced as depicted in the right portion of fig. 14. If $R_{\rm pr}(V_0, V) > \frac{L_{\rm target} - R_0}{\cos\theta_0}$ then the recoil is scattered into the 1st stopper material and new time $t(V)$ and projected range $R_{\rm pr}(V)$ functions have to be calculated, where the velocity vector has at the border between the two layers the value $V_{\rm b}$ but it has generally a different direction due to multiple scattering. This procedure is the same for the 2nd stopper material and is stopped when the γ-quantum is detected.

The main problem in the framework of this scheme is how to take into account the multiple scattering of the recoils. If only electronic stopping is considered, the slowing down process can be regarded as smooth and the direction of the recoil velocity $\boldsymbol{V}$ is conserved. The consideration of multiple scattering during the stopping process leads to the following distribution of the correlation function $\rho(v, \phi)$ for the velocity $\boldsymbol{v}$ of the scattered recoil which has a scattering angle ϕ with respect to the vector $\boldsymbol{V}$:

$$\frac{\partial^2\rho(v,\phi)}{\partial v \partial\phi} = \delta(v - V) \cdot \delta(\phi),$$

where $\delta(x)$ is a δ-function. The multiple scattering of the recoils connected with the nuclear stopping mechanism leads to a spread of the vector $\boldsymbol{v}$ around $\boldsymbol{V}$, moreover v and ϕ should be correlated. The multiple-scattering effect can be taken into account in Monte Carlo simulation calculations of the recoil trajectories including ion-atomic collisions but for high initial recoil velocities, where the total number of interactions is very large, this method becomes ineffective. Under these conditions good results can be obtained by using an approximation in which the correlation function $\rho(v, \phi)$ is separated in two factors [13,25, 26]:

$$\frac{\partial^2\rho(v,\phi)}{\partial v \partial\phi} = \delta(v - V) \cdot \frac{{\rm d}\rho(V, V_0, \phi)}{{\rm d}\phi}.$$

The angular distribution function $\frac{{\rm d}\rho(V,V_0,\phi)}{{\rm d}\phi}$ can be calculated from the diffusion equation as a superposition of Legendre polynomials, but in practice it is only possible to calculate the first [27] and, under some conditions, second [25] moments. The first moment, which is usually referred to as mean cosine Blaugrund approximation [27], can be calculated as

$$\overline{\cos\phi_{\rm Bl}}(V_0, V) = \frac{f(V)}{f(V_0)} \qquad \text{with} \quad f(V) = e^{-G\cdot I(V)}\,,$$

where G is a parameter depending on the atomic masses of the recoiling nucleus and the stopping material and

$$I(V) = \int_0^V \left[\frac{{\rm d}E}{{\rm d}x}(V)\right]_{\rm n} \cdot \left[\frac{{\rm d}E}{{\rm d}x}(V)\right]^{-1} \frac{{\rm d}V}{V}\,.$$

The calculation of $\overline{\cos\phi_{\rm Bl}}(V_0, V)$ is sufficient, to take into account multiple-scattering effects in the $F(\tau)$ method but for the correct calculation of Doppler-broadened lineshapes at least a suitable model function for $\frac{{\rm d}\rho(V,V_0,\phi)}{{\rm d}\phi}$ has to be introduced [13]. This function should reveal the Gaussian asymptotic behaviour at $V \to V_0$:

$$\left(\frac{{\rm d}\rho(V, V_0, \phi)}{{\rm d}\phi}\right)_{\rm model} \sim \exp\left[-\frac{\phi^2}{2\sigma^2(V, V_0)}\right]$$

(Gaudsmit-Saunderson limit) and satisfy the condition that $\overline{\cos\phi}(V_0, V)$ calculated with the model function is

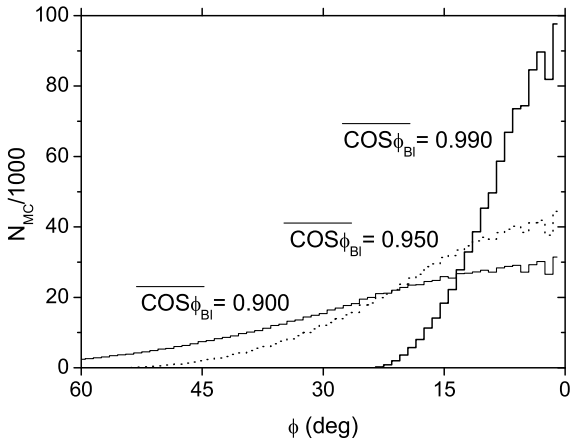

Fig. 15. Simulation of the distribution of multiple-scattering events $N_{\mathrm{m.s.}}$ as a function of the scattering angle ϕ for different values of $\overline{\cos\phi_{\mathrm{Bl}}}(V_0, V)$ in the framework of the model described in the text.

equal to $\overline{\cos\phi_{\mathrm{Bl}}}(V_0, V)$. In the program GAMMA the following function is used:

$$\left(\frac{\mathrm{d}\rho(V, V_0, \phi)}{\mathrm{d}\phi}\right)_{\mathrm{model}} = N \cdot \exp\left[-\frac{\sin^2(\phi/2)}{2\sigma^2(V, V_0)}\right]$$

$$\text{with} \quad 2\sigma^2(V, V_0) = 1 - \overline{\cos\phi_{\mathrm{Bl}}}(V_0, V)$$

In the Monte Carlo realization $\sin(\phi/2) = x$ is simulated as $x = \sigma\,\xi$, where ξ is a Gaussian-distributed random number. If $x \leq 1$ then the event is accepted and $\phi = \arccos(1-2x^2)$, otherwise a new random number will be chosen. Simulated distributions of multiple-scattering events are shown in fig. 15.

This approach works well if ϕ is sufficiently small (cf. fig. 15). Therefore, the total projected range is subdivided into parts ΔR_i and their lengths is chosen such that the change of $\overline{\cos\phi_{\mathrm{Bl}}}(V_0, V)$ is small. When this value is reduced by a factor of 0.99 a new part ΔR_i is started. Its length can be ≈ 100 to 200 μg/cm^2 at high recoil velocities and reduces to 20 μg/cm^2 for low recoil velocities. After the recoils pass a few parts, the recoil velocities are randomized and the results become practically equivalent to the simulation of each ion-atomic collision. The described approach is at least 100 times more efficient than the simulation of each collision and allows in a few minutes to perform calculations of the array $I(y, \tau_i)$ with a statistics of 10^5 events for each spectrum, ensuring a high accuracy in the fitting of experimental lineshapes.

References

1. B. Singh, R. Zywina, R.B. Firestone, Nucl. Data Sheets **97**, 241 (2002).
2. S. Lunardi, L.H. Zhu, C.M. Petrache, D. Bazzacco, N.H. Medina, M.A. Rizzuto, C. Rossi-Alvarez, G. de Angelis, G. Maron, D.R. Napoli, S. Utzelmann, W. Gast, R.M. Lieder, A. Georgiev, F. Xu, R. Wyss, Nucl. Phys. A **618**, 238 (1997).
3. R.M. Lieder, T. Rząca-Urban, H.J. Jensen, W. Gast, A. Georgiev, H. Jäger, E. van der Meer, Ch. Droste, T. Morek, D. Bazzacco, S. Lunardi, R. Menegazzo, C.M. Petrache, C. Rossi Alvarez, C.A. Ur, G. de Angelis, D.R. Napoli, Ts. Venkova, R. Wyss, Nucl. Phys. A **671**, 52 (2000).
4. R.M. Lieder, T. Rząca-Urban, H. Brands, W. Gast, H.M. Jäger, L. Mihailescu, Z. Marcinkowska, W. Urban, T. Morek, Ch. Droste, P. Szymański, S. Chmel, D. Bazzacco, G. Falconi, R. Menegazzo, S. Lunardi, C. Rossi Alvarez, G. de Angelis, E. Farnea, A. Gadea, D.R. Napoli, Z. Podolyak, Ts. Venkova, R. Wyss, Eur. Phys. J. A **13**, 297 (2002).
5. W. Starzecki, G. de Angelis, B. Rubio, J. Styczen, K. Zuber, H. Güven, W. Urban, W. Gast, P. Kleinheinz, S. Lunardi, F. Soramel, A. Facco, C. Signorini, M. Morando, W. Meczynski, A.M. Stefanini, G. Fortuna, Phys. Lett. B **200**, 419 (1988).
6. R. Ma, D.B. Fossan, E.S. Paul, N. Xu, R.J. Poynter, P.H. Regan, R. Wadsworth, Y.-J. He, I. Jenkins, M.S. Metcalfe, S.M. Mullins, P.J. Nolan, J. Phys. G **16**, 1233 (1990).
7. E.S. Paul, S.A. Forbes, D.B. Fossan, J. Gizon, J.R. Hughes, S.M. Mullins, M.S. Metcalfe, P.J. Nolan, R.J. Poynter, P.H. Regan, G. Smith, R. Wadsworth, Phys. G **18**, 121 (1992).
8. T. Rząca-Urban, S. Utzelmann, K. Strähle, R.M. Lieder, W. Gast, A. Georgiev, D. Kutchin, G. Marti, K. Spohr, P. von Brentano, J. Eberth, A. Dewald, J. Theuerkauf, I. Wiedenhöfer, K.O. Zell, K.H. Maier, H. Grawe, J. Heese, H. Kluge, W. Urban, R. Wyss, Nucl. Phys. A **579**, 319 (1994).
9. R.M. Lieder, in *Experimental Techniques in Nuclear Physics*, edited by D.N. Poenaru, W. Greiner (Walter de Gruyter, Berlin, 1997) p. 137.
10. W. Urban, Manchester University, Nuclear Physics Report 1991-1992, p. 95.
11. A.A. Pasternak, R.M. Lieder, E.O. Podsvirova, W. Gast, H. Jäger, L. Mihailescu, D. Bazzacco, S. Lunardi, R. Menegazzo, C. Rossi Alvarez, G. de Angelis, D.R. Napoli, T. Rząca-Urban, W. Urban, Laboratori Nazionali di Legnaro Annu. Rep. 2001, p. 44, web edition: `www.lnl.infn.it`; *Investigation of fold distributions for residual nuclei produced in the* $^{114}Cd+\,^{36}S$, $^{100}Mo+\,^{48}Ti$ *and* $^{97}Mo+\,^{51}V$ *reactions*, to be published in Eur. Phys. J. A.
12. T. Rząca-Urban, A. Pasternak, R.M. Lieder, W. Urban, M. Rejmund, Z. Marcinkowska, R. Marcinkowski, S. Utzelman, H.J. Jensen, W. Gast, H. Jäger, D. Bazzacco, S. Lunardi, N.H. Medina, R. Menegazzo, P. Pavan, C.M. Petrache, C. Rossi Alvarez, G. de Angelis, D.R. Napoli, L. Zhu, A. Dewald, S. Kasemann, Nucl. Phys. A **677**, 25 (2000).
13. I.Kh. Lemberg, A.A. Pasternak, *Modern Methods of Nuclear Spectroscopy* (Nauka, Leningrad, 1985).
14. J. Srebrny, Ch. Droste, T. Morek, K. Starosta, A.A. Wasilewski, A.A. Pasternak, E.O. Podsvirova, Yu.N. Lobach, G.H. Hagemann, S. Juutinen, M. Piiparinen, S. Törmänen, A. Virtanen, Nucl. Phys. A **683**, 21 (2001).

15. P. Petkov, D. Tonev, J. Gableske, A. Dewald, P. von Brentano, Nucl. Instrum. Methods A **437**, 274 (1999).
16. A.A. Pasternak, Y. Sasaki, A.D. Efimov, V.M. Mikhailov, T. Hayakawa, Y. Toh, M. Oshima, Y. Hatsukawa, J. Katakura, Z. Liu, K. Furuno, Eur. Phys. J. A **9**, 293 (2000).
17. F. Brandolini, R. Ribas, Nucl. Instrum. Methods A **417**, 150 (1998).
18. E. Grodner, Ch. Droste, T. Morek, J. Srebrny, M. Kowalczyk, A.A. Pasternak, A.A. Wasilewski, W. Płóciennik, R. Kaczarowski, E. Ruchowska, M. Kisieliński, J. Kownacki, A. Kordyasz, M. Wolińska, submitted to Phys. Rev. C (2003).
19. A.A. Pasternak, J. Srebrny, A.D. Efimov, V.M. Mikhailov, E.O. Podsvirova, Ch. Droste, T. Morek, S.Juutinen, G.H. Hagemann, M. Piiparinen, S. Törmänen, A. Virtanen, Eur. Phys. J. A **13**, 435 (2002).
20. M. Piiparinen, A. Ataç, J. Blomqvist, G.B. Hagemann, B. Herskind, R. Julin, S. Juutinen, A. Lampinen, J. Nyberg, G. Sletten, P. Tikkanen, S. Törmänen, A. Virtanen, R. Wyss, Nucl. Phys. A **605**, 191 (1996).
21. I. Hamamoto, Phys. Lett. B **193**, 399 (1987) and private communication (2003).
22. A. Arima, F. Iachello, Ann. Phys. (N.Y.) **111**, 201 (1978).
23. A.A. Pasternak, R.M. Lieder, E.O. Podsvirova, W. Gast, H. Jäger, L. Mihailescu, D. Bazzacco, S. Lunardi, R. Menegazzo, C. Rossi Alvarez, G. de Angelis, D.R. Napoli, K. Siwek-Wilczynska, Laboratori Nazionali di Legnaro Annu. Rep. 2002, p. 17, web edition: `www.lnl.infn.it`.
24. P. Petkov, D. Tonev, A. Dewald, P. von Brentano, Nucl. Instrum. Methods A **488**, 555 (2002).
25. K.I. Erokhina, I.K. Lemberg, A.A. Pasternak, Nucl. Instrum. Methods **118**, 373 (1974).
26. I.K. Lemberg, A.A. Pasternak, Nucl. Instrum. Methods **140**, 71 (1977).
27. A.E. Blaugrund, Nucl. Phys. **88**, 501 (1966).